Advance Access publication 2024 April 18

Downloaded from https://academic.oup.com/mnras/article/530/4/3906/7651291 by guest on 17 September 2024

A low-mass helium star progenitor model for the Type Ibn SN 2020nxt

Qinan Wang [®], ^{1*} Anika Goel, ^{2,3} Luc Dessart [®], ⁴ Ori D. Fox [®], ² Melissa Shahbandeh [®], ^{1,2} Sofia Rest, ⁵ Armin Rest [®], ^{1,2} Jose H. Groh, ⁶ Andrew Allan [®], ⁶ Claes Fransson [®], ⁷ Nathan Smith [®], ⁸ Griffin Hosseinzadeh [®], ⁸ Alexei V. Filippenko [®], ⁹ Jennifer Andrews [®], ¹⁰ K. Azalee Bostroem [®], ^{8*} Thomas G. Brink [®], ⁹† Peter Brown [®], ^{11,12} Jamison Burke [®], ^{13,14} Roger Chevalier [®], ¹⁵ Geoffrey C. Clayton [®], ¹⁶ Mi Dai [®], ¹ Kyle W. Davis [®], ¹⁷ Ryan J. Foley [®], ¹⁷ Sebastian Gomez [®], ¹ Chelsea Harris [®], ¹⁸ Daichi Hiramatsu [®], ^{19,20} D. Andrew Howell [®], ^{13,14} Connor Jennings, ⁹ Saurabh W. Jha [®], ²¹ Mansi M. Kasliwal [®], ²² Patrick L. Kelly [®], ²³ Erik C. Kool [®], ⁷ Evelyn Liu, ⁹ Emily Ma, ⁹ Curtis McCully [®], ¹³ Adam M. Miller [®], ^{24,25} Yukei Murakami [®], ^{1,9} Estefania Padilla Gonzalez [®], ^{13,14} Craig Pellegrino [®], ^{13,14} Derek Perera [®], ⁹ Justin Pierel [®], ² César Rojas-Bravo [®], ¹⁷ Matthew R. Siebert [®], ² Jesper Sollerman [®], ⁷ Tamás Szalai [®], ^{26,27} Samaporn Tinyanont [®], ²⁸ Schuyler D. Van Dyk [®], ²⁹ WeiKang Zheng [®], ⁹‡ Kenneth C. Chambers [®], ³⁰ David A. Coulter [®], ¹⁷ Thomas de Boer [®], ³⁰ Nicholas Earl [®], ³¹ Diego Farias [®], ³² Christa Gall [®], ³² Peter McGill [®], ¹⁷ Conor L. Ransome [®], ³³ Kirsty Taggart [®], ³¹ and V. Ashley Villar [®], ³³

Affiliations are listed at the end of the paper

Accepted 2024 March 7. Received 2024 March 6; in original form 2023 May 8

ABSTRACT

A growing number of supernovae (SNe) are now known to exhibit evidence for significant interaction with a dense, pre-existing, circumstellar medium (CSM). SNe Ibn comprise one such class that can be characterized by both rapidly evolving light curves and persistent narrow He I lines. The origin of such a dense CSM in these systems remains a pressing question, specifically concerning the progenitor system and mass-loss mechanism. In this paper, we present multiwavelength data of the Type Ibn SN 2020nxt, including *HST*/STIS ultraviolet spectra. We fit the data with recently updated CMFGEN models designed to handle configurations for SNe Ibn. The UV coverage yields strong constraints on the energetics and, when combined with the CMFGEN models, offer new insight on potential progenitor systems. We find the most successful model is a $\leq 4 \text{ M}_{\odot}$ helium star that lost its $\sim 1 \text{ M}_{\odot}$ He-rich envelope in the years preceding core collapse. We also consider viable alternatives, such as a He white dwarf merger. Ultimately, we conclude at least some SNe Ibn do not arise from single, massive ($> 30 \text{ M}_{\odot}$) Wolf–Rayet-like stars.

Key words: circumstellar matter – supernovae: individual: SN 2020nxt – ultraviolet: general – transients: supernovae.

1 INTRODUCTION

Core-collapse supernovae (CCSNe) are the explosive endpoint of massive stars' lives. These stars typically explode in relatively low-density environments that have been self-cleared by stellar radiation pressure and low-density winds prior to explosion. A growing number of transients, however, have now been observed to explode in a high-density, slow-moving, circumstellar medium (CSM) likely generated by progenitor pre-SN mass-loss on the order of 10^{-3} – 10^{-1} M $_{\odot}$ yr $^{-1}$ (Smith 2017). These pre-shocked, high-density winds emit relatively narrow ($\lesssim 1000 \, \text{km s}^{-1}$) lines, adding

an 'n' classification to the subclass (e.g. SNe IIn, Ibn; Schlegel 1990; Filippenko 1997; Smith 2017, and references therein).

SNe Ibn (see Pastorello et al. 2008a and Hosseinzadeh et al. 2017 for reviews) is one such CCSN subclass that exhibits hydrogen-poor (e.g. stripped-envelope Type Ib) spectra dominated by narrow He I emission lines. Their optical light curves are distinct from those of normal SNe Ib given their high peak luminosity and fast rise/decline. In the case of the SNe Ibn 2006jc and 2019uo, imaging observations reveal a pre-SN outburst, potentially an extreme mass-loss event, \sim 2 yr prior to explosion that may have been the origin of the CSM (Pastorello et al. 2007; Strotjohann et al. 2021).

Fox & Smith (2019) first proposed a potential connection between SNe Ibn and another puzzling subclass named Fast Blue Optical Transients (FBOTs), in particular AT 2018cow (Margutti et al. 2019). These extreme transients are defined by their light curves' relatively fast rise and decline (<10 d above half-maximum), high peak bolometric luminosity ($>10^{44}$ erg s⁻¹), and blue colour (e.g.

^{*} E-mail: qwang75@jhu.edu

^{*} LSSTC Catalyst Fellow.

[†] Draper-Wood-Robertson Specialist in Astronomy

[‡] Bengier-Winslow-Eustace Specialist in Astronomy

Drout et al. 2014). Almost all FBOTs also show narrow lines and signs of interaction with CSM, although there is also evidence that at least some are powered by a central engine (e.g. Yao et al. 2022; Chen et al. 2023; Ho et al. 2023). Ho et al. (2021) provide a thorough review, noting that there may really be at least two distinct groups: (1) at the lower energy end, the more common SNe Ibn (hydrogenpoor stripped-envelope Type Ibn-like), and (2) at the high-energy end, the much less frequent FBOTs (e.g. AT2018cow; Margutti et al. 2019). There may even be other types of fast transients with signs of CSM intetaction connected to these groups, such as the H-poor and He-poor Type Icn SNe (Davis et al. 2022; Gal-Yam et al. 2022; Pellegrino et al. 2022; Perley et al. 2022).

SNe Ibn, SNe Icn, and FBOTs invoke a number of questions specific to our understanding of stellar evolution and explosions. For many stripped-envelope SNe, two of the most common progentior systems proposed are a single massive Wolf-Rayet (WR) star with a high mass-loss rate (e.g. Gaskell et al. 1986; Pastorello et al. 2007; Smith, Foley & Filippenko 2008; Pastorello et al. 2008b, 2015a, b, c) or a close binary system (Podsiadlowski, Joss & Hsu 1992). Earlier studies of the Type Ibn SN 2006jc suggested the dense CSM was formed by a strong wind from a massive WR progenitor (e.g. Foley et al. 2007; Pastorello et al. 2007). This single, massive WR star model, however, is problematic (Dessart, John Hillier & Kuncarayakti 2022). Most known physical mechanisms for normal stellar winds, particularly for single stars, are insufficient to produce the inferred mass-loss rates in SNe Ibn (e.g. Smith 2014). Theory predicts that a standard WR star explosion with inner shell decelerated by CSM down to speeds of \sim 2000 km s⁻¹ should yield a superluminous SN (Dessart et al. 2016; Dessart et al. 2022), but SNe Ibn like SN 2006jc only have peak luminosities of $L_{\rm peak} \approx$ 10⁴³ erg s⁻¹, at least an order of magnitude fainter than SLSNe. Also, the presence of He I lines at all times requires a He-dominated CSM composition, which is directly incompatible with most massive WR-star models.

Instead, such massive CSMs require eruptive mass-loss akin to luminous blue variables (Smith et al. 2011) or pre-SN binary interaction (Smith & Arnett 2014) may be required. Late-time *Hubble Space Telescope (HST)* imaging of SN Ibn explosion sites indicate that at least some SNe Ibn do not originate from high-mass stars (Hosseinzadeh et al. 2019; Sun et al. 2020). Shivvers et al. (2017) use pre-explosion images to rule out a WR progenitor for the Type Ibn SN 2015G (Shivvers et al. 2017). Progenitor masses of $\lesssim 12$ M_{\odot} are further constrained by local stellar population studies (Sun, Maund & Crowther 2023). Furthermore, modelling of Type Ibn spectra (Dessart et al. 2022) showed that Type Ibn SN progenitors have final masses of only $\lesssim 5~M_{\odot}$, much lower than those for WR stars.

Recently, the theoretical community has proposed a wide range of new physical scenarios. Binary models are successful at explaining at least some of the observed CSM characteristics of SNe Ibn by invoking nuclear flashes in low-mass He stars (Woosley 2019; Dessart et al. 2022) or repeated mass-transfer episodes in short-period binaries (Pols 1994; Dewi & Pols 2003; Langer 2012; Tauris et al. 2013). Other proposed explosion models include a double white dwarf merger (Lyutikov & Toonen 2019; Dessart et al. 2022; Metzger 2022), a Thorne–Zytkow-like object (TZIO) as a result of head-on collision between white dwarf and neutron star (NS) collapse to an NS or a black hole as a central engine (see Paschalidis et al. 2011), a millisecond-period magnetar powering an ultrarelativistic gamma-ray-burst jet (e.g. Metzger et al. 2011), and other potential extreme scenarios, such as intermediate-mass black holes (e.g. Perley et al. 2022).

Ultimately, not all SNe Ibn are homogeneous. There are peculiar SNe Ibn (e.g. very slowly rising objects; see Karamehmetoglu et al. 2021) that may challenge theoretical models. Furthermore, the class of FBOTs is an observationally defined sample, and as such it is perhaps unlikely that they all come from the same progenitor channel. Whether or not multiple mechanisms are at work, more observations are needed to make any connection between this variety of mechanisms and progenitors and the diversity of SNe Ibn. Given the large number of possible interaction configurations, one may even expect a continuum of events covering the parameter space from SNe Ibn/Icn to FBOTs (e.g. Dessart et al. 2022). Stellar evolution, in particular if one invokes binarity, can produce a large set of evolutionary paths.

Unlike many of the other SN subclasses, SNe Ibn do not yet have direct observational evidence of their quiescent progenitor systems. Instead, the community has had to rely on indirect evidence, mostly consisting of optical spectroscopy/photometry and host-galaxy studies (Hosseinzadeh et al. 2019, and those within). These observations have highlighted the need for multiwavelength, multi-epoch observations, especially in the ultraviolet (UV) (e.g. Dessart et al. 2022). The bolometric light curve, built from UV, optical, and near-infrared (NIR) observations, is essential to constrain the energy budget of these transients and identify a multicomponent emission source. In addition, the degeneracy in the light-curve properties requires the additional wealth of information encoded in spectra (e.g. composition, line-profile properties such as morphology, width, or strength).

In this paper, we present multiwavelength observations of SN Ibn 2020nxt, including UV, optical, and NIR. Section 2 presents the observations, while Section 3 discusses the modelling of the spectral series. In Section 3.4, we examine line diagnostics and their implications for the progenitor system and evolution channel. Finally, Section 4 provides the conclusion of our work and implications for the future. Throughout the paper, we adopt a flat ΛCDM cosmological model with $H_0=73~km~s^{-1}~Mpc^{-1}$ and $\Omega_m=0.27$ (Riess et al. 2022).

2 OBSERVATIONS

SN 2020nxt was first discovered by the Asteroid Terrestrial-impact Last Alert System (ATLAS; Tonry et al. 2018a) on 2020 July 3 12:53:16.8 UTC (MJD 59033.537) in the o band with $m_o =$ 17.192 mag (Tonry et al. 2020), and was spectroscopically classified as an SN Ibn on July 14 with the Liverpool Telescope (Srivastav et al. 2020). The last non-detection on SN 2020nxt was on 2020 July 1 14:29:46 UTC (MJD 59031.604) with a limiting magnitude $m_o \lesssim 19.67$. We adopt a redshift of $z = 0.0218 \pm 0.003$ measured from the centroid of He I λ 7065 through all phases. This corresponds to a distance of 91.1 \pm 1.2 Mpc and a distance modulus of μ = 34.798 ± 0.032 mag. The Milky Way extinction is relatively low towards this direction, with $E(B - V)_{MW} = 0.067$ mag (Schlafly & Finkbeiner 2011). The peak of ATLAS o band is on MJD 59039.485 with $m_{o,\text{peak}} = 15.985$ mag. We applied a quadratic fit to the ATLAS o-band light curve from MJD 59 035 to 59 045 and estimated the o-band peak to be on 2020 July 8 18:14:24 UTC (MJD 59038.76).

2.1 UV, optical, near-IR imaging

The ATLAS images are processed as described by Tonry et al. (2018a), and then photometrically and astrometrically calibrated using the RefCat2 catalogue (Tonry et al. 2018b). Template generation, image-subtraction procedures, and photometric measurements are

carried out following Smith et al. (2020). The ATLAS light curves are then cleaned, averaged, and converted into AB magnitude system using a suite of routines described by Rest et al. (2021). The first cut uses the χ^2 and uncertainty values of the point-spread-function (PSF) fitting to clean out bad data. We then obtain forced photometry of 8 control light curves located in a circular pattern around the SN with a radius of 17 arcsec. The flux of these control light curves is expected to be consistent with zero within the uncertainties and any deviation from that would indicate that there are either unaccounted systematics or underestimated uncertainties. We search for such deviations by calculating the 3σ cut weighted mean of the set of control light-curve measurements for a given epoch (for a more detailed discussion, see Rest et al. in preparation). The weighted mean of these photometric measurements is expected to be consistent with zero and, if not, we flag and remove those epochs from the SN light curve. This method allows us to identify potentially bad measurements in the SN light curve without using the SN light curve itself. We then bin the SN 2020nxt light curve by calculating a 3σ cut weighted mean for each night (typically, ATLAS has 4 epochs per night), excluding the flagged measurements from the previous step. We find that this method successfully removes outliers from the SN light curve.

Follow-up observations of SN 2020nxt were also performed by the 0.76 m Katzman Automatic Imaging Telescope (KAIT) as part of the Lick Observatory Supernova Search (LOSS; Filippenko et al. 2001), as well as the 1 m Nickel telescope at Lick Observatory. B, V, R, and I multiband images of SN 2020nxt were obtained with both telescopes, and additional *Clear*-band images (close to the *R* band; see Li et al. 2003) were obtained with KAIT. All images were reduced using a custom pipeline² detailed by Stahl et al. (2019). The image-subtraction procedure was applied in order to remove the host-galaxy light, using additional images obtained after the SN had faded below our detection limit. PSF photometry was obtained using DAOPHOT (Stetson 1987) from the IDL Astronomy User's Library. Several nearby stars were chosen from the Pan-STARRS1⁴ catalogue for calibration; their magnitudes were first transformed into the Landolt (Landolt 1992) system using the empirical prescription presented by equation (6) of Tonry et al. (2012), and then transformed to the KAIT/Nickel natural system. Apparent magnitudes were all measured in the KAIT4/Nickel2 natural system. The final results were transformed to the standard system using local calibrators and colour terms for KAIT4 and Nickel2 (Stahl et al. 2019).

SN 2020nxt was observed with Las Cumbres Observatory (Brown et al. 2013) as part of the Global Supernova Project, using the Sinistro camera on the 1 m telescope at McDonald Observatory (TX, USA) and the Spectral camera on the 2 m Faulkes Telescope North (FTN) at Haleakalā Observatory (H I, USA). These images were pre-processed using BANZAI (McCully et al. 2018). We subtracted reference images taken with the same 1 m telescope on 2022 September 17 UTC using PyZOGY (Guevel & Hosseinzadeh 2017) and measured PSF photometry on the difference images using lcogtsnpipe (Valenti et al. 2016). *UBV* Vega magnitudes are calibrated to Landolt (1983) standard fields taken on the same nights with the same telescopes, and *gri* AB (Oke & Gunn 1983) magnitudes are calibrated to the Sloan Digital Sky Survey (SDSS; SDSS Collaboration 2017).

We also observed SN 2023bee with the PanSTARRS1 (PS1) telescope (Chambers et al. 2016) in *griz* bands as part of the Young Supernova Experiment (Jones et al. 2021a; Aleo et al. 2022). The PS1 images are reduced by the PS1 Image Processing Pipeline (IPP; Waters et al. 2020; Magnier et al. 2020a, b, c), and then calibrated using the Pan-STARRS DR1 catalogue (Flewelling et al. 2020).

UV and additional optical imaging was performed with the *Neil Gehrels Swift Observatory* (Gehrels et al. 2004; Roming et al. 2005). Observations began on 2020 July 16 at 02:38:13 UTC. Reductions were performed using the methods outlined by Brown et al. (2009) and the pipeline of the *Swift* Optical Ultraviolet Supernova Archive (SOUSA; Brown et al. 2014). The count-rate flux from the host galaxy within the source aperture was subtracted using an observation on 2021 January 22.

The multiband light curves are shown in Fig. 1. We further use the SUPERBOL pipeline (Nicholl 2018) to calculate the bolometric light curve from Lick, ATLAS, and *Swift* light curves, as shown in Fig. 2. In order to align measurements in different filters on the same epochs, we use the *B* band as the reference filter and interpolate and extrapolate the light curves in other bands with second-order polynomials between MJD 59 045 and 59065. We then estimate the full bolometric light curve by fitting a black-body SED. For the later phases when no UV data are present, we also calculated the pseudo-bolometric light curve by integrating the photometry in *BVRI* bands as a reference to the bolometric luminosity evolution, as shown in Fig. 2.

2.2 Host galaxy

SN 2020nxt exploded 4.5 arcsec (2.0 kpc projected) west of the spiral galaxy WISEA J223736.70 + 350006.5. Following the methodology of Hosseinzadeh et al. (2019), we downloaded a u^\prime -band image of this galaxy from the SDSS Collaboration 2017 and measured the surface brightness within a 5 pixel \times 5 pixel (0.9 kpc \times 0.9 kpc) aperture centred on the SN location (Fig. 3). The result, $\sigma_{u^\prime}=23.2\pm0.2$ mag arcsec $^{-2}$, implies a star formation rate (SFR) density of $\Sigma_{SFR}=0.019\,M_\odot$ yr $^{-1}$ kpc $^{-2}$, according to the relationship of Kennicutt (1998). This places the site of SN 2020nxt near the median SFR density among SN Ibn (Hosseinzadeh et al. 2019) and other CCSN (Galbany et al. 2018) hosts.

2.3 Pre-explosion imaging

Given the pre-SN outburst observed 2 yr prior to SN 2006jc (Foley et al. 2007; Pastorello et al. 2007), we searched the pre-explosion data of SN 2020nxt for a similar brightening event. ATLAS monitored the field of SN 2020nxt in the c and o bands for \sim 3 yr prior to explosion. We use the tool kit 'ATClean' (Rest et al. 2023), which was developed to clean and bin ATLAS light curves as well as search for excess flux such as outbursts in pre-SN light curves using a quantitative efficiency and contamination analysis.

As described in Section 2.1, we first obtain a set of eight forced photometry light curves around the location of SN 2020nxt. These light curves are 17 arcsec away from the SN so that they can serve as *controls* to help determine the background variation and, consequently, the detection limit of any potential outbursts in the pre-SN light curve. We use ATClean to remove bad or noisy measurements and bin both the SN and control light curves (see Section 2.1) before proceeding with our outburst search. We additionally exclude control light curve #4 because it overlaps with a bright point source. The top panel of Fig. 4 displays the cleaned and binned pre-explosion ATLAS

¹https://github.com/srest2021/atlaslc

²https://github.com/benstahl92/LOSSPhotPypeline

³http://idlastro.gsfc.nasa.gov/

⁴http://archive.stsci.edu/panstarrs/search.php

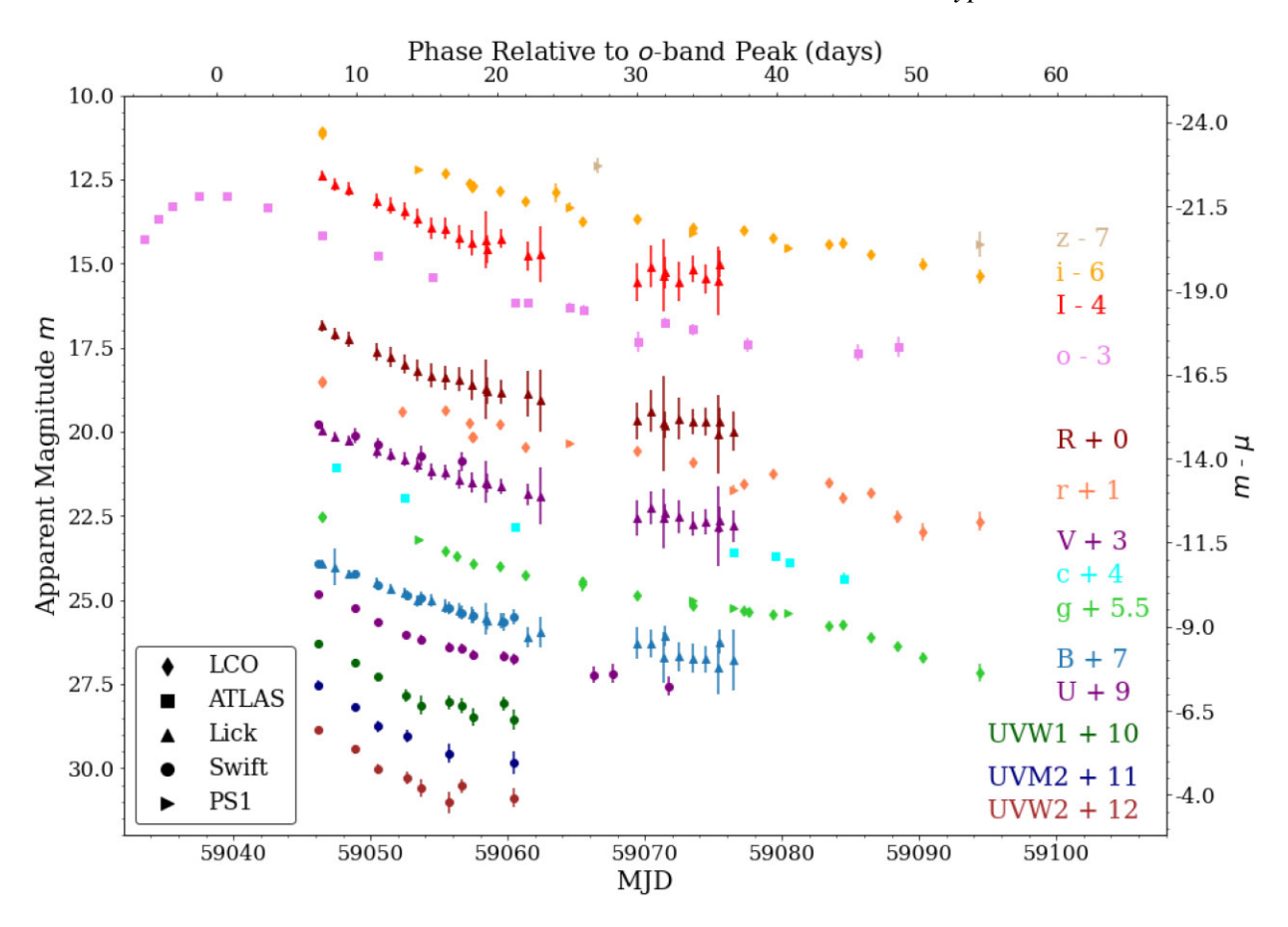


Figure 1. Multiband light curves of SN 2020nxt within the first \sim 70 d. The rest-frame phases labelled at top of the plot are relative to the inferred time of peak brightness in the ATLAS o band on MJD 59038.76. For clarity each band has been shifted as labelled in the annotations.

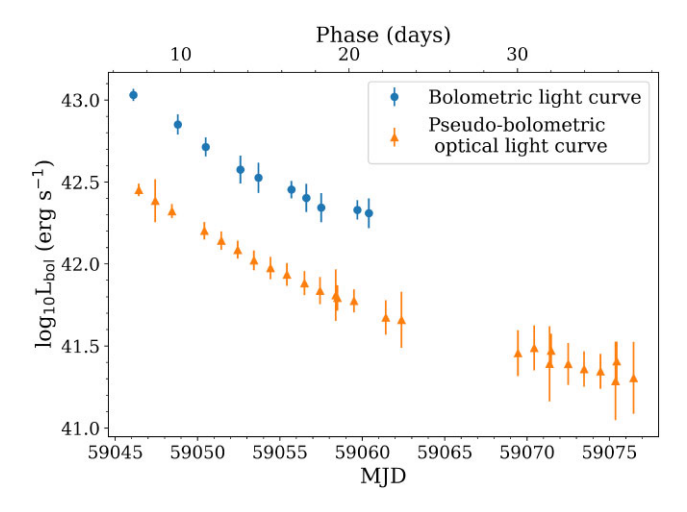


Figure 2. Bolometric and pseudo-bolometric light curves of SN 2020nxt. The bolometric light curve (blue) is estimated by fitting a blackbody SED to the UV-optical light curve when UV data from *Swift* are present. The pseudo-bolometric light curve (orange) is estimated by integrating through the *BVRI* bands as an indicator of the bolometric light-curve evolution at later phases. The phases are relative to *o*-band maximum brightness.

light curve generated by forced photometry at the position of the SN, along with its cleaned and binned control light curves.

In accordance with our primary objective to identify the presence of pre-SN outbursts in the SN 2020nxt light curve, our detection

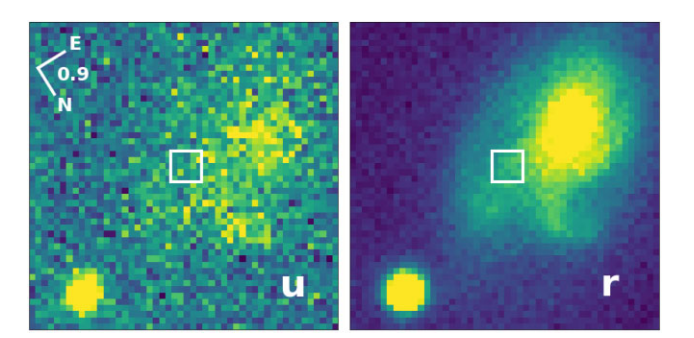


Figure 3. u'-band image (left) and r'-band image (right) of the host galaxy of SN 2020nxt. By measuring the UV flux within a 5×5 pixel 2 (0.9×0.9 kpc 2) aperture centred on the SN location (white square), we derived a surface brightness of 23.2 mag arcsec $^{-2}$ and an SFR density of $0.019 \, M_\odot \, yr^{-1} \, kpc^{-2}$, near the median for SNe Ibn (Hosseinzadeh et al. 2019).

algorithm is designed to reflect the most basic feature of these outbursts – that a real eruption adds positive flux to consecutive detections, even if its individual detections may not exceed 3σ above zero. We thus define a figure of merit (FOM; hereafter referred to as Σ_{FOM}) for our outburst detection algorithm as the flux-to-uncertainty ratio convolved with a rolling Gaussian of kernel size σ_{kernel} . This convolution, when applied to a binned ATLAS light curve, will emphasize the signal of any real (though faint) eruption. Most importantly, the rolling Gaussian with a kernel size σ_{kernel} can best amplify the target pre-SN outburst signal with similar time-scale.

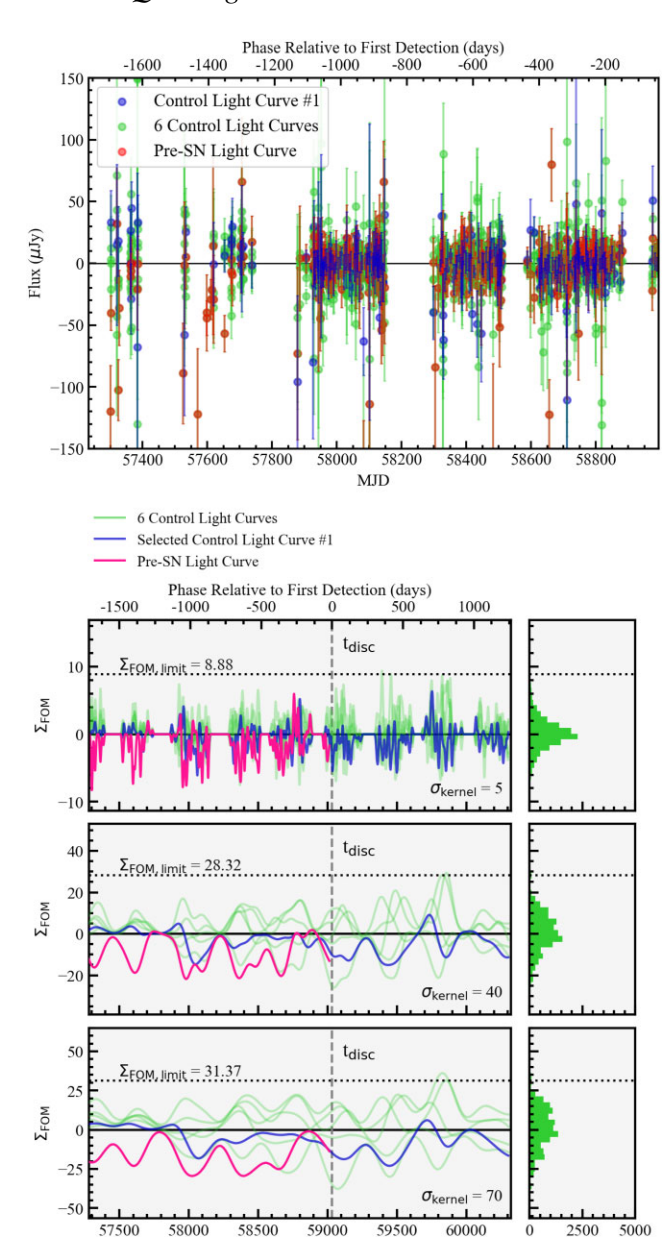


Figure 4. *Top:* The pre-SN light curve (red) in the *o* band compared with the control light curves (green) taken from the background around the position of SN 2020nxt through all phases. One of the control light curves has been highlighted (blue) for clarity and comparison. *Bottom:* To the left, the weighted sum of the S/N convolved with a rolling Gaussian with kernel sizes $\sigma_{\text{kernel}} = 5$, 20, and 40 d. The horizontal dotted lines denote the detection limits $\Sigma_{\text{FOM,limit}}$ of the corresponding σ_{kernel} , as determined by the frequency distribution of the control light curve Σ_{FOM} , shown in the right panels. The vertical dashed lines denote the time of discovery.

We display Σ_{FOM} for the pre-SN and control light curves, along with histograms of the Σ_{FOM} distributions, for three kernel sizes of interest in the bottom panels of Fig. 4.

To determine whether a detection is real, or set upper limits for non-detections, we must establish an optimal detection limit $\Sigma_{FOM,limit}$ for each kernel size σ_{kernel} in advance of running the algorithm on the pre-SN light curve. In doing so, we aim to account for contamination caused by factors such as instrument and reduction artefacts or nearby bright objects, while simultaneously remaining sensitive to faint

eruptions. As our control light curves allow us to assume the absence of any real astrophysical flux, we can refer to them to calculate diagnostic measures such as *efficiency* (i.e. the success rate of the ATClean outburst detection algorithm on pre-SN outburst events simulated within these control light curves) and *contamination* (i.e. the amount of false positives by the detection algorithm using a certain detection limit).

As discussed by Rest et al. (in preparation) and depicted in the Σ_{FOM} histograms of Fig. 4, the Σ_{FOM} distribution is not guaranteed to be Gaussian-shaped, particularly for $\sigma_{kernel} >$ 40 d. As such, instead of using the classic σ -cut method to determine the detection limits, we set the aforementioned controlled measures of contamination to a constant value across each σ_{kernel} , then compute the detection limits which best satisfy this criterion. We define our target contamination value for the corresponding $\Sigma_{FOM,limit}$ to be 1 (falsely) positive control light curve (i.e. at most one continuous sequence of Σ_{FOM} rises above $\Sigma_{FOM,limit}$). In the bottom panels of Fig. 4, we display the computed detection limits $\Sigma_{FOM,limit}$ for the kernel sizes of interest in relation to the pre-SN and control Σ_{FOM} . Note how the Σ_{FOM} distributions for larger kernel sizes become increasingly less Gaussian-shaped, further emphasizing the need for meaningful detection limits

We now determine the efficiency of our detection algorithm using the previously established detection limits by calculating the detection success of many series of simulated outbursts. The first integral step in achieving this goal is to simulate and inject an event into a control light curve so that we can apply the detection algorithm; in order to do so, we model the target pre-SN outbursts with Gaussians of varying size $\sigma_{\rm sim}$ and peak apparent magnitude $m_{\rm peak}$. Fig. 5 displays an example of a simulated event with $\sigma_{\rm sim}=20$ d and $m_{\rm peak}=21.5$ mag injected into an example control light curve. For four kernel sizes of interest, we display the original $\Sigma_{\rm FOM}$ in blue and the simulated $\Sigma_{\rm FOM}$ in purple. Evidently, for all kernel sizes, the simulated $\Sigma_{\rm FOM}$ surpasses the corresponding $\Sigma_{\rm FOM,limit}$ and the algorithm successfully detects the simulated event.

We aim to analyse the efficiency of the following rolling Gaussian kernel sizes: $\sigma_{\text{kernel}} = 5, 20, 40, 70, 100, \text{ and } 150 \text{ d.}$ For each σ_{kernel} , we inject simulated Gaussian events with similar σ_{sim} and calculate the rate of successful algorithmic detection. As eruptions typically have time-scales of σ_{eruption} between \sim 5 and 100 d (Ofek et al. 2014; Strotjohann et al. 2021; Jacobson-Galán et al. 2022), we set the possible σ_{sim} values to 5, 20, 40, 70, 100, and 150 d, including the kernel size of 150 d for completeness. We draw m_{peak} from a possible range of 16-23 mag and randomly draw the peak MJD from the observation seasons (we exclude the first two observation seasons MJD < 57 876 owing to bad cadence). Each simulated event is injected into a randomly drawn control light curve, which is then scanned for $\Sigma_{FOM} > \Sigma_{FOM,limit}$ within 1σ of the peak MJD. We simulate and inject a total of 50 000 events. Then, we calculate the efficiency (i.e. the percent of successfully detected simulations) of each σ_{kernel} with respect to simulation σ_{sim} and m_{peak} .

Lastly, we compute the peak apparent magnitudes at which each efficiency curve crosses 50 per cent and 80 per cent to get apparent magnitude thresholds $m_{\rm threshold}$. In Fig. 6, we display $m_{\rm threshold}$ across our range of $\sigma_{\rm sim}$ for different $\sigma_{\rm kernel}$. Evidently, we can conclude that with an 80 per cent efficiency goal, we can set an upper limit of $m_{\rm threshold}=19.8$ mag or $M_{\rm threshold}=-15$ mag for short pre-explosion eruptions with 5 d durations, and $m_{\rm threshold}=21.3$ mag or $M_{\rm threshold}=-13.5$ mag for long pre-explosion eruptions with 100 d durations in the case of SN 2020nxt. No significant detection is identified at

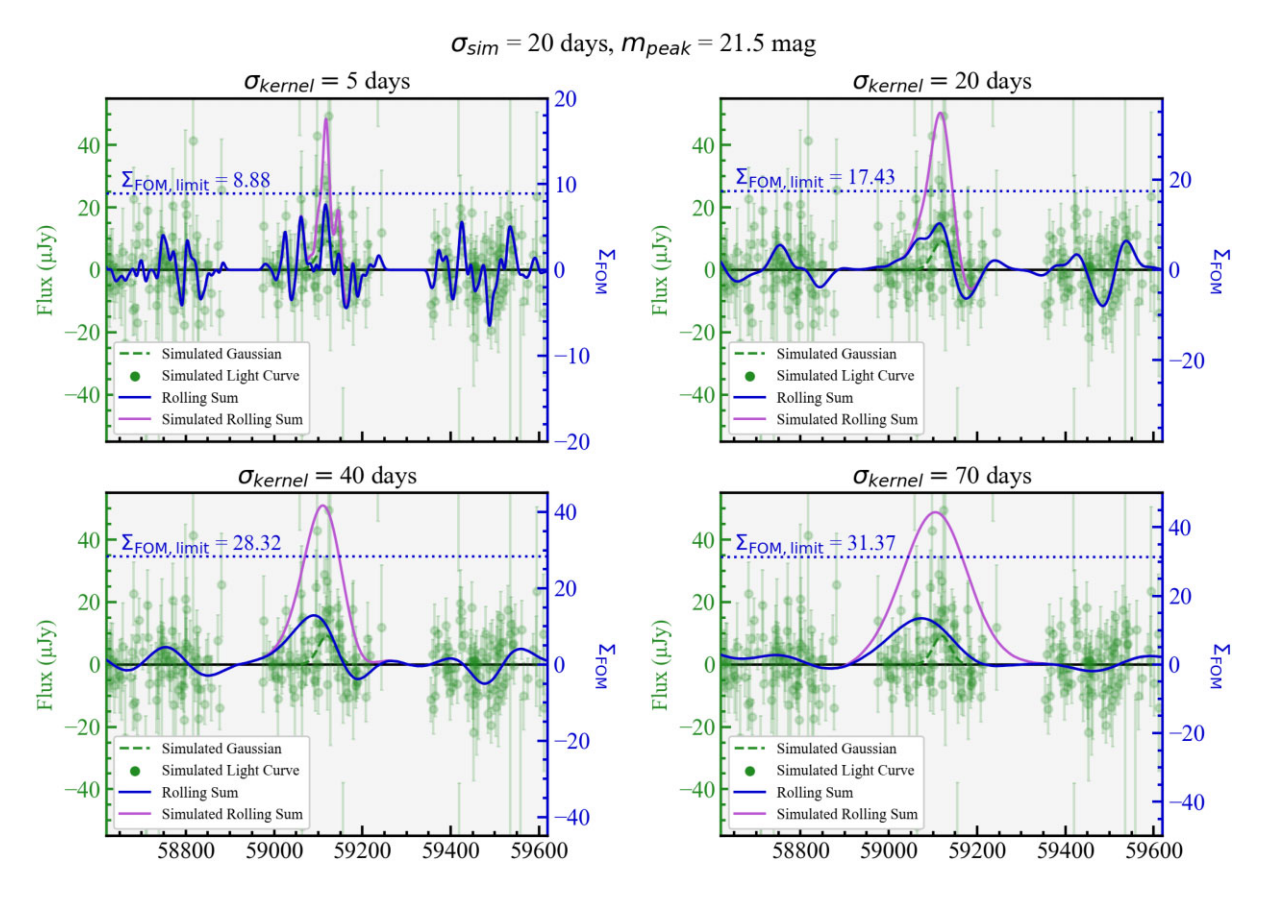


Figure 5. The same simulated Gaussian event, with $\sigma_{sim}=20$ d and $m_{peak}=21.5$ mag, injected into an example control light curve and convolved with four rolling Gaussians of different kernel sizes: $\sigma_{kernel}=5$ d (top left), 20 d (top right), 40 d (bottom left), and 70 d (bottom right). In the green points, the control light curve flux after injection of the simulated event. In the dashed green line, the shape of the injected Gaussian event. In the solid blue line, the original Σ_{FOM} . In the solid purple line, the Σ_{FOM} after injection of the simulated event. The simulated Σ_{FOM} successfully crosses the detection limit $\Sigma_{FOM,limit}$ (dashed blue line) for all four σ_{kernel} .

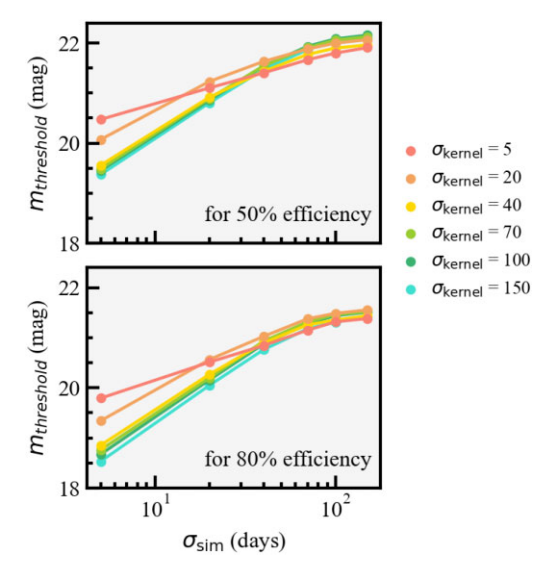


Figure 6. The relationship between the threshold magnitude $m_{\rm threshold}$ and the width of simulated Gaussian $\sigma_{\rm sim}$ for different size of rolling Gaussian kernel $\sigma_{\rm kern}$. Left and right panels show the corresponding threshold curves for different detection efficiency requirements. Notice that for eruptions with duration longer than \gtrsim 70 d, the threshold magnitude no longer has a strong correlation with the eruption duration.

the site of SN 2020nxt over time-scales of 5–150 d in pre-explosion ATLAS o-band data.

2.4 Optical and near-IR spectroscopy

Optical spectroscopy was obtained with several telescopes, summarized in Table 1 and plotted in Fig. 7. FLOYDS spectra from FTN were observed with a 2 arcsec-wide slit and reduced using the floyds_pipeline⁵ (Valenti et al. 2014). Observations with the Nordic Optical Telescope (NOT; Djupvik & Andersen 2010) on La Palma used the Alhambra Faint Object Spectrograph (ALFOSC).⁶ All spectra were obtained using the parallactic angle (Filippenko 1982) and with airmass <1.3. A slit width of 1".0 and Grism 4 were used for all observations. Three of the spectra have excellent signalto-noise ratio (S/N), while the fourth was affected by calima dust. The NOT spectra were reduced using the Pypeit pipeline (Prochaska et al. 2020a, b). The classification spectrum was obtained using the SPectrograph for the Rapid Acquisition of Transients (SPRAT; Piascik et al. 2014) on the 2 m Liverpool Telescope (Steele et al. 2004). SPRAT uses a 1.8 arcsec slit and covers a wavelength range of \sim 4000–8000 Å.

Additional optical spectra were obtained through the Young Supernova Experiment (YSE; Jones et al. 2021b; Coulter et al.

⁵https://github.com/LCOGT/floyds_pipeline

⁶Programmes 61.604 & 61–501, P.I. J. Sollerman

59084.6

MJD Phase (d) Telescope Instrument Grism/grating Wavelength range (Å) Resolution (Å) 59044.1 +5.3LT SPR AT 4020-7580 92 59046.5 +7.6**FLOYDS** 3500-10000 2.2 FTN 59048.4 +9.43618-10712 2.0 Shane Kast 59049.0 +10.0NOT ALFOSC 4003-9689 3.6 59049.5 +10.53306-10496 2.5 Shane Kast 59049.7 +10.7**HST** STIS G140L + G230L1138-3180 0.6/1.559052.5 **FLOYDS** 3500-10000 +13.4FTN 1.7 59053.4 +14.3Keck I LRIS 3302-10097 1.2 59055.0 +15.9NOT ALFOSC 4000-9635 3.6 +19.22.5 59058.4 Shane Kast 3616-10688 59058.7 +19.5**HST** STIS G230L 1570-3180 1.5 59061.5 +22.3FTN **FLOYDS** 3500-10000 2.3 59062.1 +22.8NOT ALFOSC 4002-9624 3.6 59065.5 +26.2FTN FLOYDS 3500-10000 1.7 59070.6 +31.2Keck I **LRIS** 3505-10493 2.5 59072.4 +32.92.0 Shane Kast 3618-10714 59074.5 +35.7Keck 2 NIRES 9650-24670 2.2 600/4000 + 400/85001.2 59083.6 +43.9Keck I LRIS 3156-10280

600/4000 + 400/8500

LRIS

Table 1. Log of spectroscopic observations of SN 2020nxt. The phases are relative to o-band maximum brightness.

2022, 2023) with the Keck-I 10 m telescope using LRIS (Oke et al. 1995), and also with the Lick 3 m (Shane) telescope using the Kast spectrograph (Miller & Stone 1993). They were reduced through the UCSC Spectral Reduction Pipeline (Siebert et al. 2020), a custom data-reduction pipeline based on procedures outlined by Foley et al. (2003), Silverman et al. (2012), and references therein. The two-dimensional (2D) spectra were bias-corrected, flatfield corrected, adjusted for varying gains across different chips and amplifiers, and trimmed. One-dimensional (1D) spectra were extracted using the optimal algorithm (Horne 1986). The spectra were wavelength-calibrated using internal comparison-lamp spectra with linear shifts applied by cross-correlating the observed nightsky lines in each spectrum to a master night-sky spectrum. Flux calibration and telluric correction were performed using standard stars at a similar airmass to that of the science exposures. We combine the sides by scaling one spectrum to match the flux of the other in the overlap region and use their error spectra to correctly weight the spectra when combining. More details of this process are discussed elsewhere (Foley et al. 2003; Silverman et al. 2012; Siebert et al. 2020: Davis et al. 2022).

+44.9

Keck I

An NIR spectrum of SN 2020nxt was obtained on 2020 Aug. 13 (MJD 59074.5) with the Near-Infrared Echellette Spectrometer (NIRES; Wilson et al. 2004) mounted on the Keck-II 10 m telescope, with slit width of 0.55 arcsec. The SN was observed in an ABBA dithering pattern for sky subtraction, and reduced utilizing the Spextool software package (Cushing, Vacca & Rayner 2004). The telluric absorption corrections were done with the XTELLCOR software. The log of NIR spectroscopic observation is given in Table 1, and the spectrum is presented in Fig. 8.

All spectral data and corresponding information will be made available via WISeREP⁸ (Yaron & Gal-Yam 2012).

2.5 HST/STIS UV spectroscopy

SN 2020nxt was observed twice with the *HST*/STIS as part of programme GO-15834 (PI: O. Fox), as summarized in Table 1

and plotted in Fig. 9. The 1D spectrum for each observation is extracted using the CALSTIS custom extraction software stistools.x1d. The default extraction parameters for STIS are defined for an isolated point source. For both G140L and G230L, the default extraction box width is 7 pixels and the background extraction box width is 5 pixels. The UV and optical spectra are then flux-calibrated to the *Swift* UVOT UVM2 and *B*-band photometry.

1.2

3202-10147

2.6 Line analysis

Most of the identified lines have been marked in Figs 7–8. In this section, we discuss the evolution of the most prominent lines. The He features are strong throughout all phases, especially He I 5876, 7065 Å. Mg II doublets around 7880 Å and 9230 Å are prominent within the first 20 d but gradually weakened and are hardly visible afterward. On the other hand, the Ca II triplet around 8600 Å is not visible at the earliest phases, but appeared ~14d after the first detection and gradually became prominent at later phases. Fig. 10 shows the selected line profiles of He I 5876, 7065 Å, Mg II doublets, and Ca II triplets throughout all phases in velocity space. Despite the change in the line flux, the variation in the centroid velocities of Ca II and He I lines are negligible. The FWHM of these lines is $\leq 2000 \,\mathrm{km} \,\mathrm{s}^{-1}$ throughout all phases. The lack of any blueward shift in the line profile combined with the absence of any NIR excess suggests that any new dust formation is relatively small. After day 20, a weak and very narrow H α feature becomes visible in some spectra, most likely originating from the host

In the far-UV, a number of highly ionized emission features are present, including Nv 1240 Å, C II 1335 Å, and the C IV resonance doublet at 1548, 1550 Å. There is another strong emission feature at 1400 Å and could originate from O IV, S IV, or Si IV. In the near-UV, the only strong features during the early phase are the Mg II doublets around 2800 Å, while C III 1907 Å and C II 2323 Å can barely be seen. In the NIR spectrum taken $+35.7\,d$ post-peak, the strongest features are the broad emission lines of He I 1.083 μm and 2.0581 μm , while other relatively weak metal emission lines including C I, Ca II, and Mg I can also be identified.

⁷https://github.com/msiebert1/UCSC_spectral_pipeline

⁸https://wiserep.weizmann.ac.il

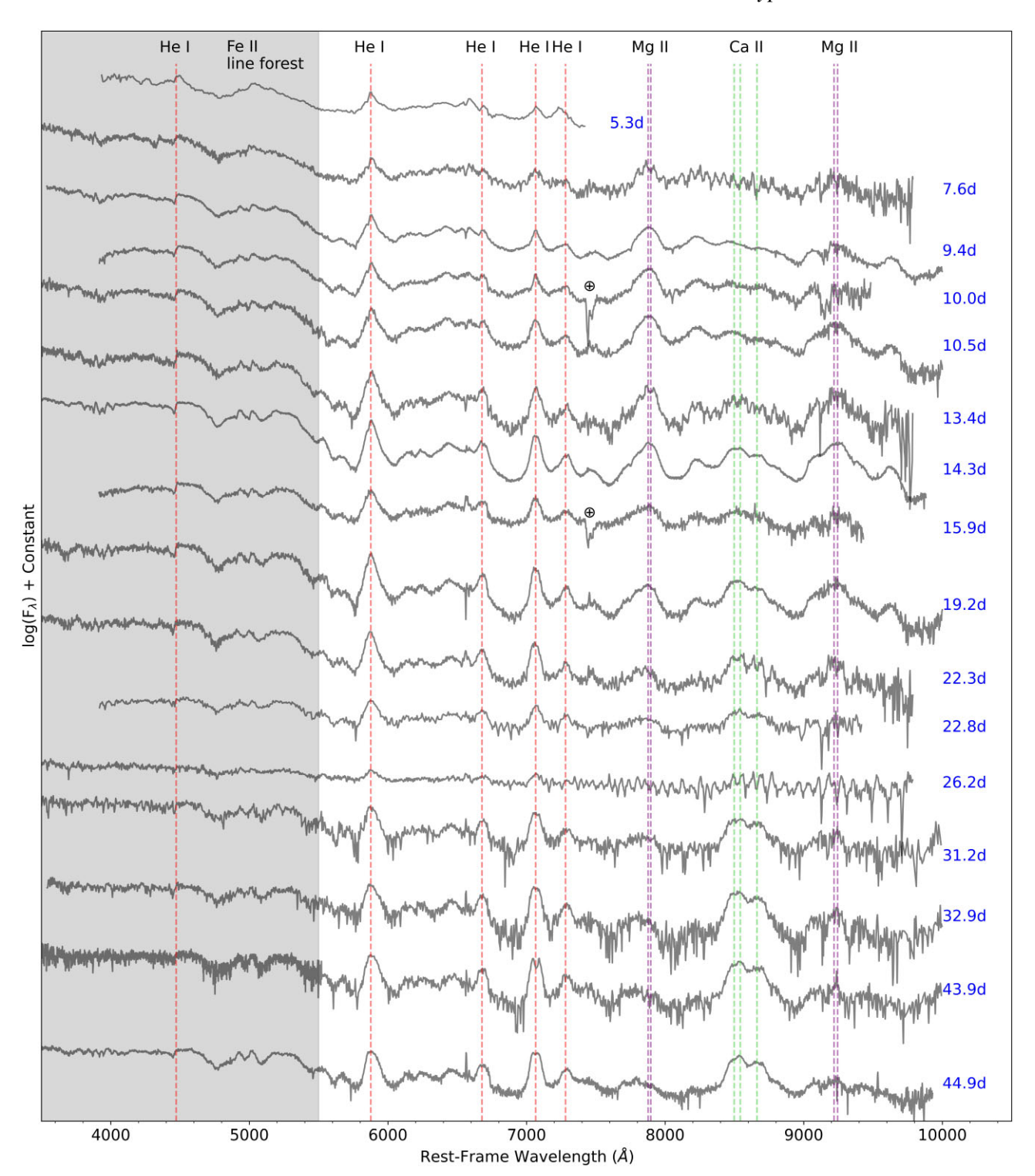


Figure 7. Optical spectral series of SN 2020nxt in the rest frame shown in log scale. Vertical dashed lines indicate the wavelengths of some of the strongest lines. The grey shadowed region below 5500 Å is dominated by the Fe II line forest and hard to identify any line features except for He I 4471 Å. All of the spectra have been normalized to the continuum in the range of 6100–6300 Å. Phases relative to the *o*-band peak at MJD 59038.76 are labelled to the right side of each spectrum. The spectra after 22.3 d are rebinned for clarity owing to their relatively low S/N.

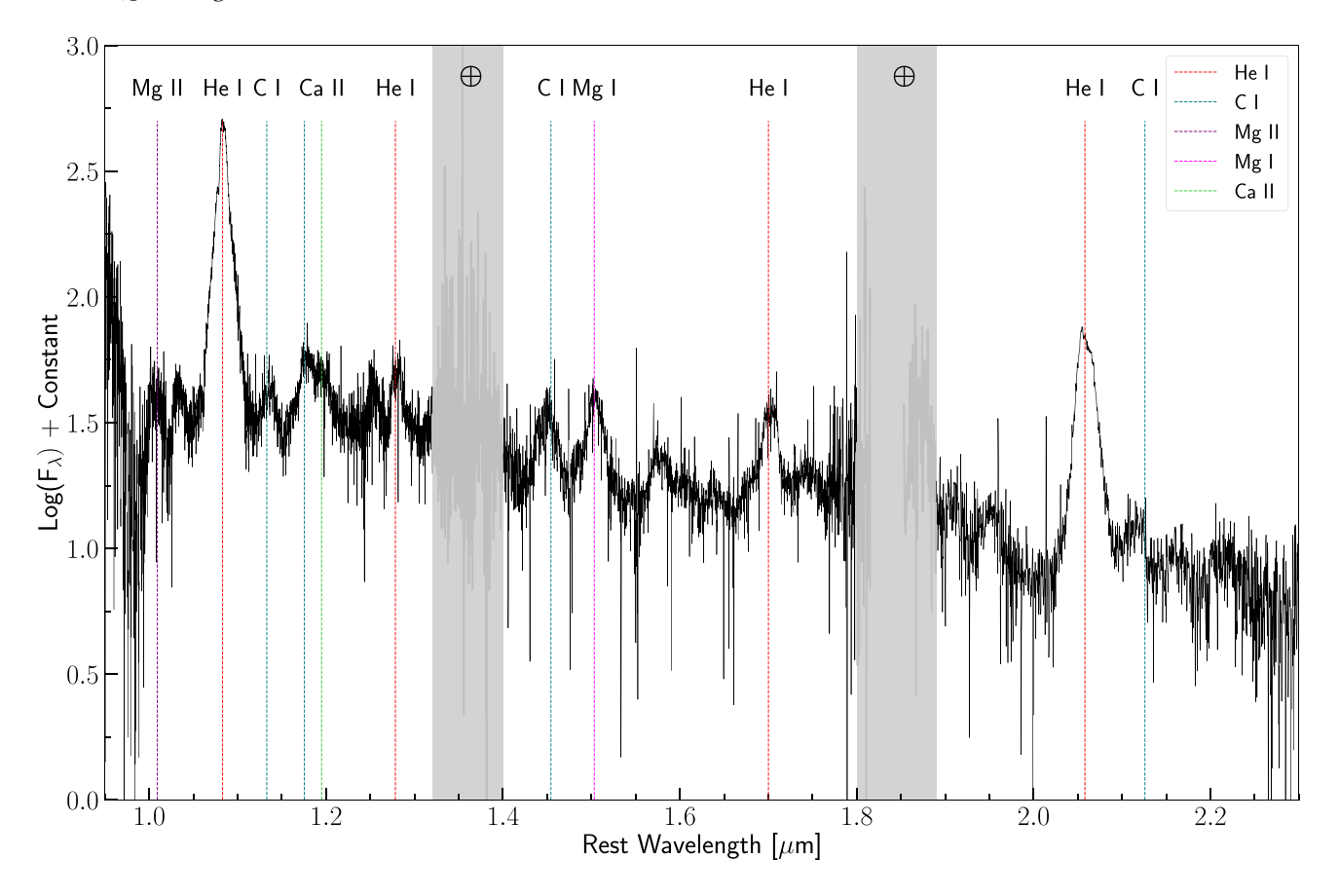


Figure 8. The NIR spectrum of SN 2020nxt obtained on 2020 Aug. 13 at phase + 35.7 days past maximum brightness with the Keck-II telescope. The two grey bands mark regions that have high telluric absorption. The flux is plotted on a log scale, and the prominent features in the spectrum are identified.

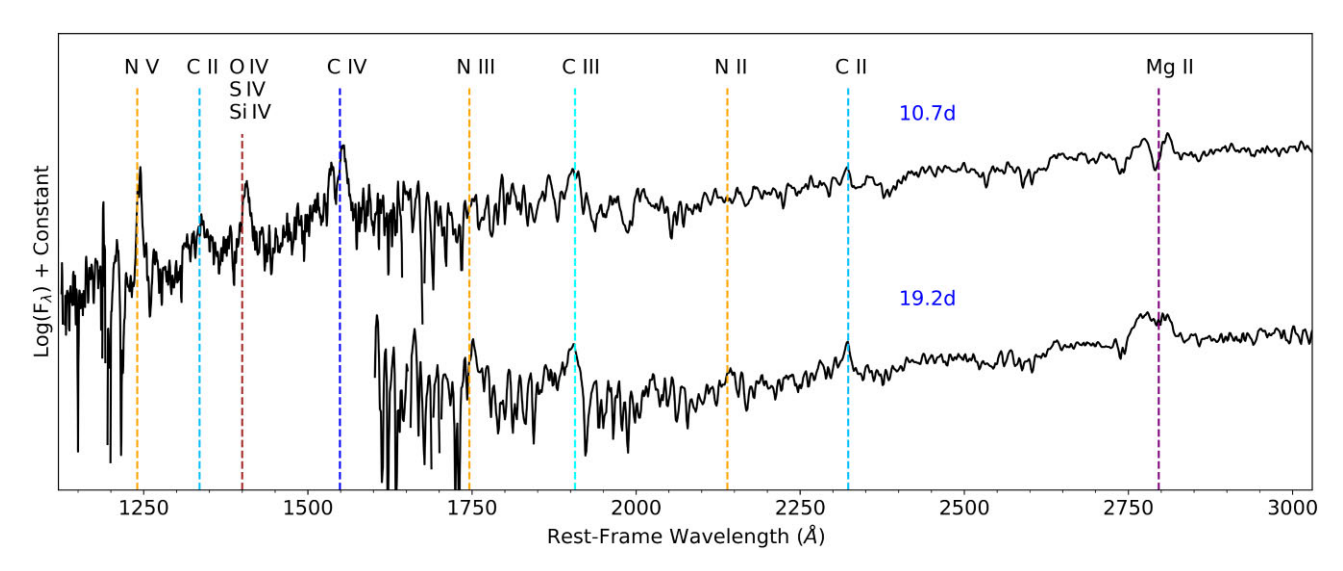


Figure 9. UV spectra of SN 2020nxt taken with *HST* STIS at phase +10.0 and +14.3 d past maximum. The spectra have been smoothed with a Gaussian kernel and plotted on a log scale for clarity, and the prominent line features are identified with vertical lines.

3 ANALYSIS

3.1 The type Ibn supernova model

In order to constrain the mass of the progenitor star and ejecta, we make a comparison between the state-of-the-art simulation with CMFGEN and our spectral series of SN 2020nxt. The radiative-

transfer simulations presented here include some of the original calculations presented by Dessart et al. (2022, hereafter D22) as well as new calculations with different parameters. For the SN Ibn scenario, the context is that of low- or moderate-energy, low-mass ejecta interacting with ${\sim}1\,M_{\odot}$ He-rich CSM. The progenitor for this scenario could be a low-mass binary He-rich star losing its Herich envelope just before core collapse, followed by the evolution

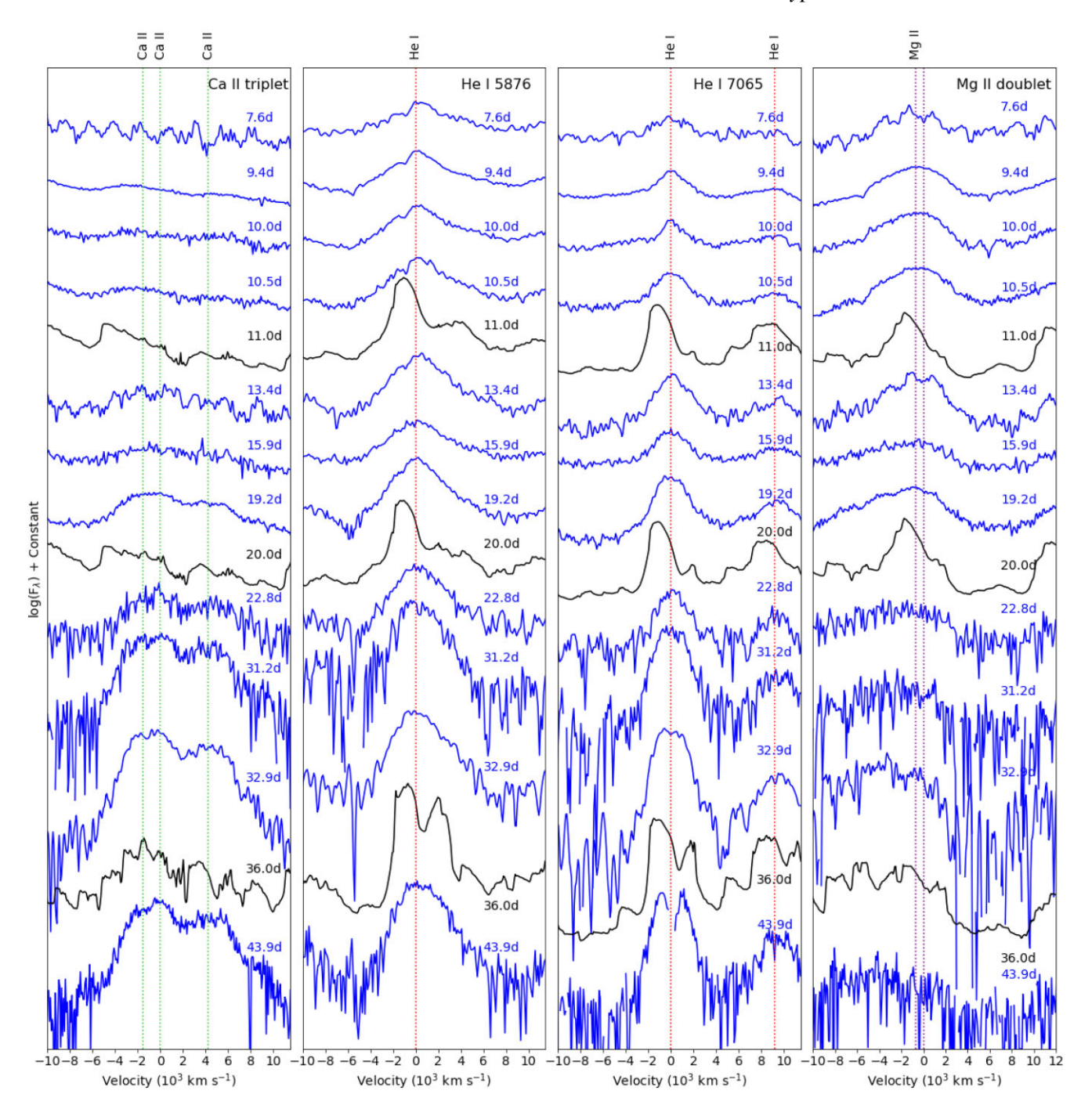


Figure 10. The profiles of He I 5876, 7065 Å, Mg II doublet around 7891 Å, and Ca II triplet around 8542 Å from observed (blue) and theoretical (black) spectra, plotted in velocity space. Spectra are normalized to the 6100–6300 Å continuum. Prominent features are marked with vertical dashed lines. Phases are labelled near each spectrum.

of the remaining star until core collapse and a weak neutrino-driven explosion – such events are predicted from stellar-evolution models in this mass range (Woosley 2019). This envelope loss could arise, for example, through a Case BB unstable mass-transfer episode (Pols 1994; Dewi & Pols 2003) or through a nuclear flash as may arise in single or binary stars having a small core mass (Woosley & Heger 2015; Woosley 2019). Our numerical approach applies best after bolometric maximum light, when the inner and outer shells have been essentially entirely swept up (i.e. the interaction is essentially over) into a dense narrow shell (i.e. $\delta V/V \ll 1$, where V is the ejecta

velocity) that evolves in a quasi-steady state and expands ballistically while the power arises from the residual interaction. In this work, we treat directly the interaction shock power in the radiative transfer with CMFGEN to better accounting for greater non-local thermodynamic equilibrium (NLTE) effects, H-deficient interactions and stronger role played by lines, under which the methodology in the study of SN 1994W do not work well (Dessart, Audit & Hillier 2015; Dessart et al. 2016). With this approach, we lose a little on the the physical consistency of the treatment on hydrodynamics, but we gain

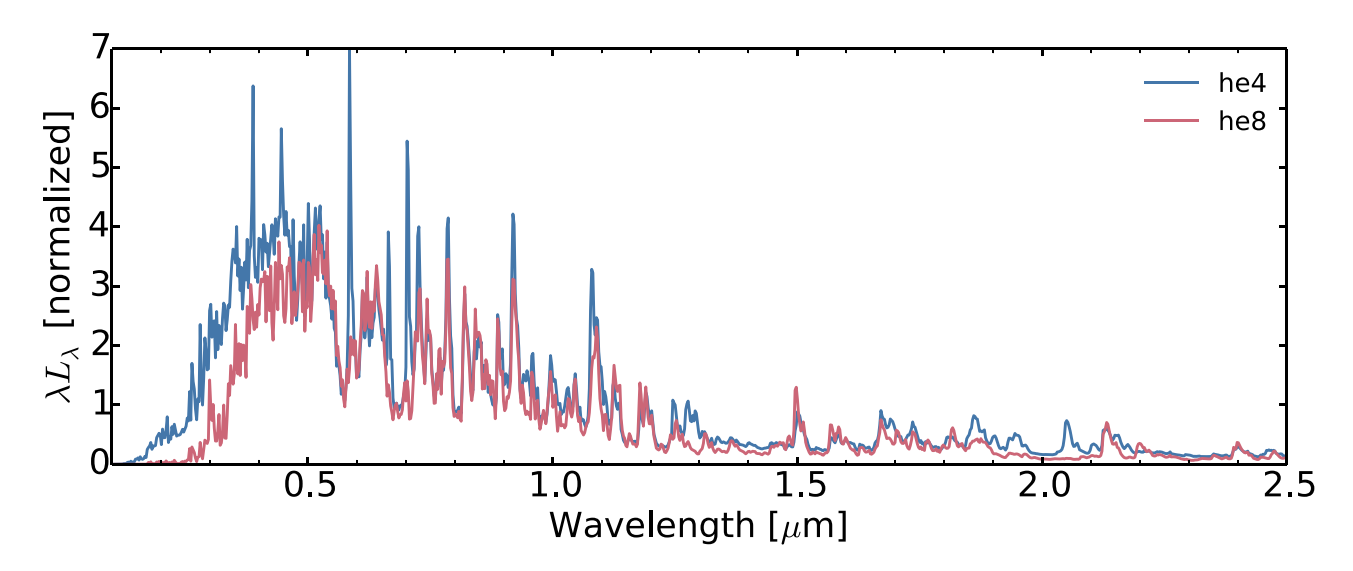


Figure 11. Two different model spectra illustrating the impact of the He content and ejecta mass on the SED for a dense shell moving at 2000 km s⁻¹, located at a radius of 3×10^{15} cm and with an injected power of 2×10^{42} erg s⁻¹. The models shown are he4 (total mass of $1.62 \, \mathrm{M_{\odot}}$, with $0.92 \, \mathrm{M_{\odot}}$ of He) and he8 (total mass of $3.95 \, \mathrm{M_{\odot}}$, with $0.84 \, \mathrm{M_{\odot}}$ of He) from D22. The model with higher mass and lower He content shows weak or no He I lines (e.g. at 3888, 4471, 5875, 6678, 7065, 10 830, or 20 581 Å) and exhibits extra blanketing in the blue (mostly because of the greater mass but identical power).

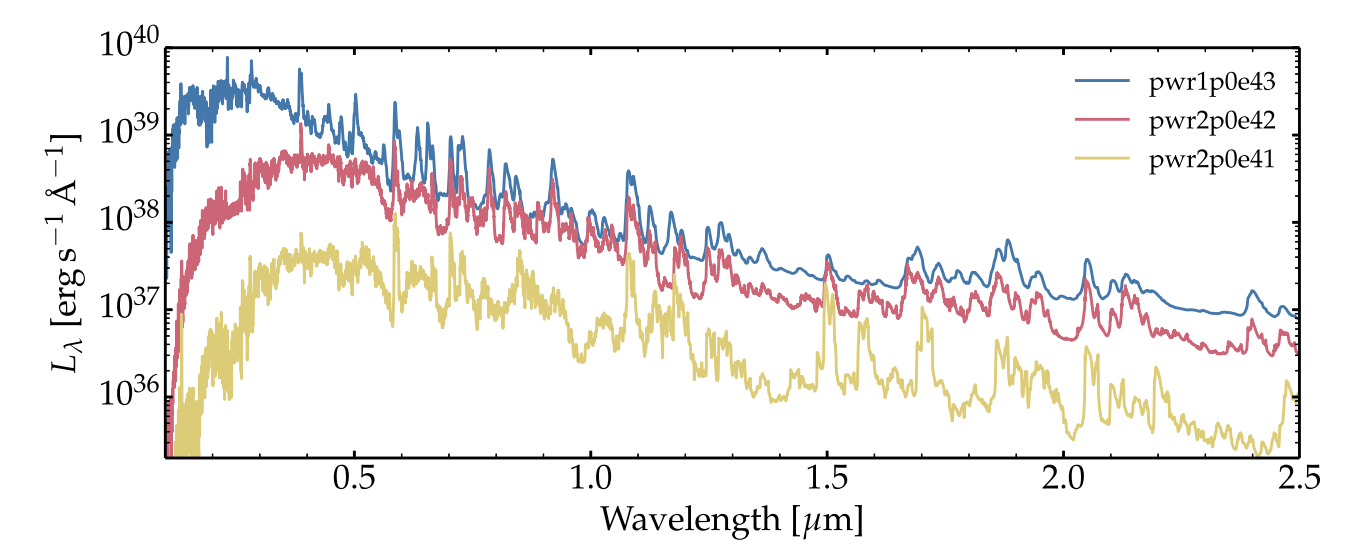


Figure 12. Grid of interaction calculations based on the he4p0 model, a radius of 3×10^{15} cm, and a velocity of $2000 \,\mathrm{km} \,\mathrm{s}^{-1}$ with powers of 2×10^{41} , 2×10^{42} , and $10^{43} \,\mathrm{erg} \,\mathrm{s}^{-1}$. With decreasing power, the ionization of the dense shell gets lower and continuum gets weaker especially in the UV region.

significantly on the treatment of the gas and the interaction between radiation and matter.

A further assumption of D22 is to treat the shock power released in the complicated, inherently 3D interaction region in a similar way to the γ -ray energy deposition from decay power. In practice, the model injects the power within the dense shell and ignores any distinction between the relative contributions from the reverse and forward shocks. That is, it focuses on that part of the total shock power that is thermalized within the dense shell (this might be 1 per cent, 10 per cent, or 100 per cent of the total power produced by the shock) and injects that power in the form of high-energy electrons. Then, using the non-thermal solver in CMFGEN, the model computes the degradation of these high-energy electrons as they collide with electrons, ions, and atoms in the plasma. From this degradation spectrum, the influence of non-thermal electrons on the temperature, ionization, and excitation is

determined. The overall approach in CMFGEN is therefore analogous to the treatment of radioactive decay in models of standard SNe.

Other models for interacting SNe have been produced by Groh (2014) with CMFGEN, but in this case use a radiative-transfer solver adapted for the conditions of optically thick stellar winds. In this 'stellar wind' approach, one assumes a steady-state configuration with a prescribed luminosity at a diffusing inner boundary layer, an optically thick medium at that inner boundary, and an overlying steady flow that reprocesses the impinging continuum flux. However, these assumptions are not well suited for SNe Ibn at most epochs. As discussed by D22, the physical conditions post-maximum brightness in SNe Ibn suggest an optically thin nebula cooling through a forest of Fe II lines and a negligible contribution from continuum processes apart from the far-UV range. The observations also suggest the presence of low-velocity dense material (probably in a dense shell

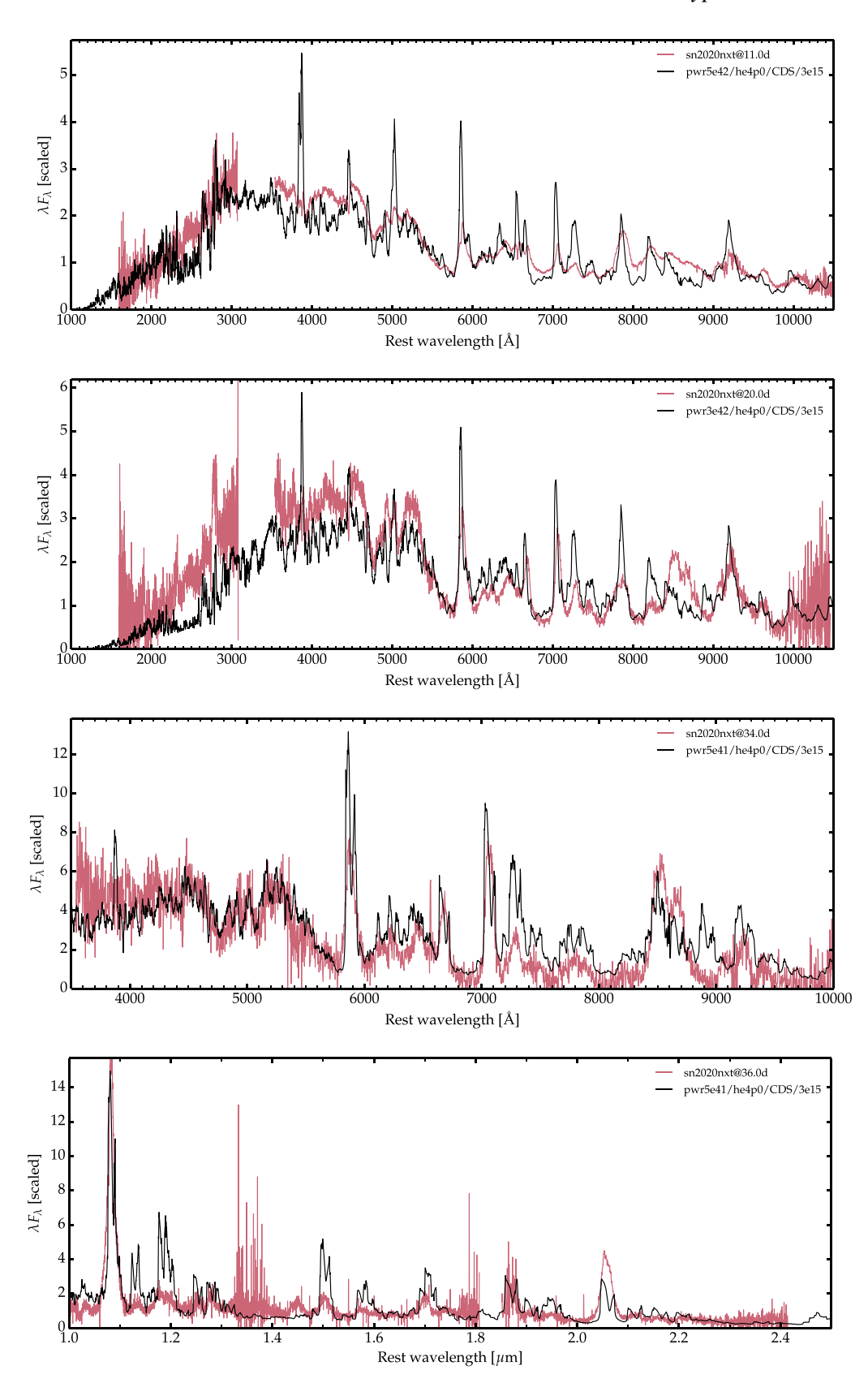


Figure 13. Comparison of he4 models and multiwavelength spectra of SN 2020nxt at 11, 20, 34, and 36 d after *o*-band maximum brightness. The top two panels combine *HST/UV* and optical data calibrated to contemporarneous photometry.

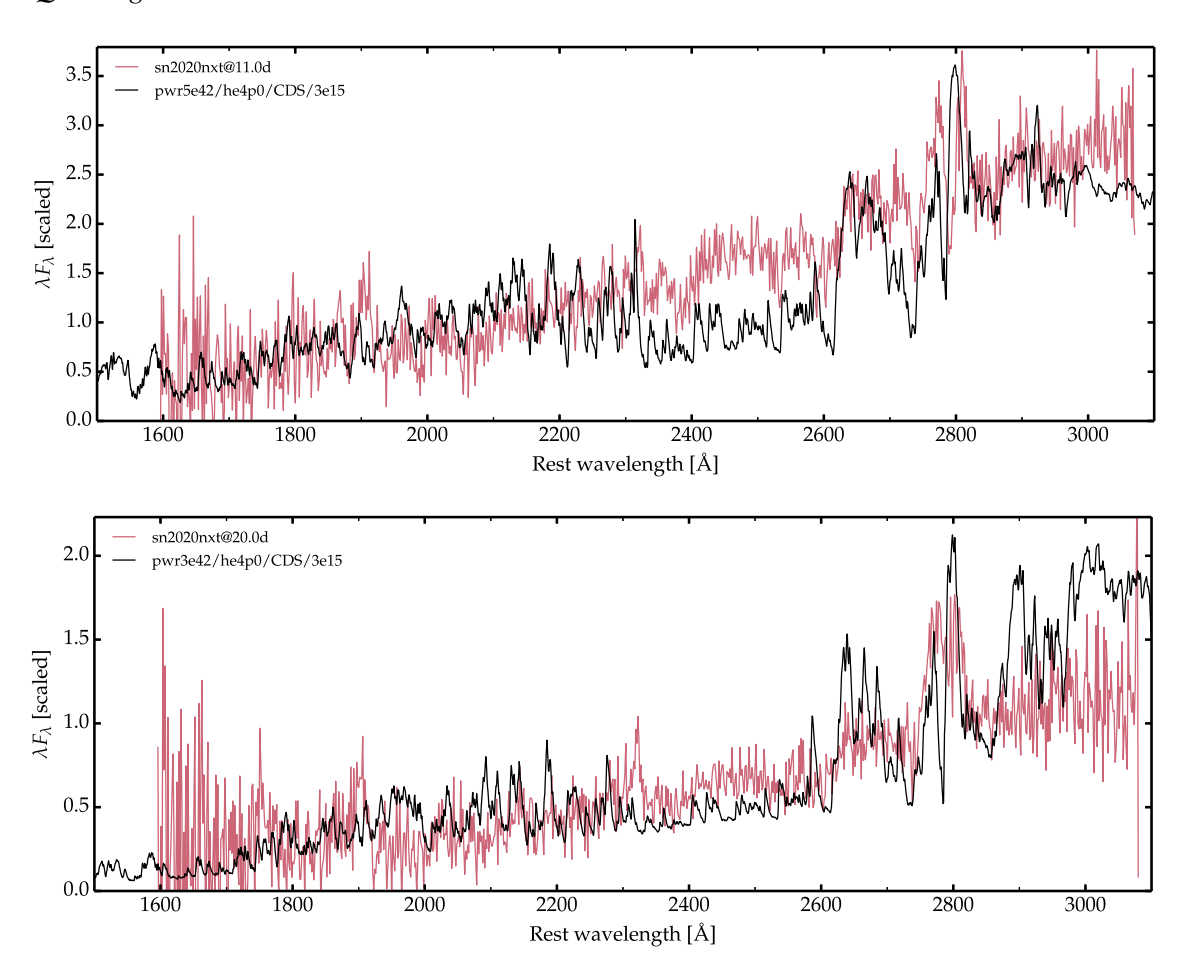


Figure 14. Same as Fig. 13 but with UV spectra only.

formed from the interaction between ejecta and CSM) and powered by a shock (D22). The power originates from within the interaction region rather than being exterior to it. This interaction is also marginally optically thin and thus a non-LTE treatment is preferred. Under these assumptions, the radiative-transfer calculations with CMFGEN reproduce satisfactorily the observed spectra of SNe Ibn (D22).

Because of the spectral similarity between SN 2020nxt and the SNe Ibn discussed by D22, we use similar He-rich models. The presence of He I lines at all times suggests a He-rich progenitor. Woosley (2019) shows that the persistent presence of He I lines in SNe Ibn like SN 2020nxt excludes high-mass progenitors, instead corresponding to a He-star model with an initial mass on the He zero-age main sequence (ZAMS) of $\lesssim 4 \,\mathrm{M}_{\odot}$. For reference, Fig. 11 shows the UV and NIR spectra of models based on the composition of a He star explosion from a progenitor that had 4 or 8 M_{\infty} initially on the He ZAMS, i.e. the he4 and he8 models. All the material from this He-star model is then placed within a narrow, dense shell, with a profile given by a Gaussian centred on a velocity of 2000 km s⁻¹ and a characteristic width of 70 km s⁻¹. While the persistent presence of He I lines in SNe Ibn like SN 2020nxt excludes high-mass progenitors such as model he8, any model with about 50 per cent He mass fraction seems suitable. In the He-star models of Woosley (2019), this suggests that models he3 (i.e. a He star progenitor of 3 M_o initially on the He ZAMS) to he4 are adequate; we choose the he4 model for the present study. This model is characterized by a total mass of $1.62\,M_{\odot}$, with $0.92\,M_{\odot}$ of He, $0.31\,M_{\odot}$ of O, $0.03\,M_{\odot}$ of Mg, $0.0014 M_{\odot}$ of Ca, and a solar metallicity. Fig. 12 further shows the UV to NIR spectra of he4 models with different input power ranging from 2×10^{41} to 10^{43} erg $\,\rm s^{-1}$. In our simulations, we assume all the power comes from interaction and thus ignore any radioactive-decay heating.

3.2 Modelling the spectra

Fig. 13 shows a comparison between the he4 model and the spectra of SN 2020nxt at multiple epochs after bolometric maximum brightness. In particular, we highlight the comparison with the exquisite STIS UV spectra in Fig. 14. For simplicity, we use the same model for all epochs although variations in composition would reduce the discrepancy for certain lines. With increasing time, the only parameter that is changed is power, dropping from 6×10^{42} to 5×10^{41} erg s⁻¹ between 10 and 34–36 d after o-band maximum, while the dense shell is set at 3×10^{15} cm and moves at 2000 km s⁻¹. These powers are roughly compatible with the inferred bolometric light curve (Fig. 2). The radius is not firmly established, but in the similar-looking SN Ibn 2006jc a pre-SN outburst occurred 2 yr before the main explosion. So, a representative year-long time-scale with line widths suggestive of a velocity of order 1000 km s⁻¹ yields a representative radius of 3×10^{15} cm.

Given the simplifications of the approach (i.e. the dense shell, the power source, spherical symmetry, etc.), the observations are satisfactorily reproduced. In particular, the landmarks of SNe Ibn with strong Fe II line emission everywhere below 5500 Å and the myriad of He I lines is well reproduced at all epochs. Fig. 15 further shows the evolution of he ratio of the flux associated with Fe II line emission below 5500 Å and some individual He I lines. At early times after maximum brightness, our assumption of a narrow dense shell is probably the least adequate and may explain in part the overestimation of the He I line strengths (top panel of Fig. 13). At that time, the flux between lines does not drop to very small values as observed at later epochs and the contrast in flux between the blue and red parts of the optical is moderate. Our model successfully reproduce this feature by employing a greater power ($5 \times 10^{42} \, \mathrm{erg \, s^{-1}}$). Hence, relative to later epochs when the luminosity is smaller, the stronger continuum flux is caused by the greater ionization, which also causes a greater ejecta optical depth (the total Rosseland-mean optical depth $\tau_{Ross} = 2.4$).

At subsequent epochs, we adopt the bolometric luminosity inferred in Section 2.1 and the power is thus reduced, first to 3×10^{42} (20 d post-maximum) and then 5×10^{41} erg s⁻¹ (34–36 d post-maximum). With a lower power, the dense shell has a lower ionization, a smaller optical depth (τ_{Ross} is then 1.4 and 0.55, respectively), and Ca⁺ eventually dominates over Ca²⁺, causing the strengthening of the Ca II NIR triplet. This feature, never reproduced in the D22 models, may now be explained exclusively through an ionization (rather than an abundance) effect. In these models, the Mg II lines at 7896, 8234, and 9218 Å tend to be overestimated at all epochs, although we do reproduce their observed weakening with time – the strength of these Mg II lines varies between observed SNe Ibn and they eventually weaken, probably as a result of the reduction in ionization and density (which are also inferred from the strengthening of the Ca II NIR triplet). The change in these two sets of lines can be more easily seen in Fig. 15. The NIR spectrum shown in the bottom panel of Fig. 13 yields a satisfactory match to the observations of SN 2020nxt at 35.7 d, although the model tends to overestimate the strength of some metal lines, in particular those associated with CI, MgI, and MgII (the same discrepancy affects Mg II lines in optical spectra). The UV spectrum shown in Fig. 14 also yields a relatively satisfactory match including the dominant Mg II doublets around 2800 Å, though there are deviations in the continuum, likely caused by the difficulties in accurately simulating the line-blanketing effect from Fe-group elements.

There are two important discrepancies here. First, the model spectra for the first two epochs struggle to reproduce the whole UV and optical range, as well as account for the simultaneous presence of Mg II and Ca II lines. A possible solution to this discrepancy is that the spectrum forms in a more complex environment than adopted here, one that includes a broader range in density and ionization, as might be expected in a 3D interaction model. Evidence for this comes from another discrepancy in line-profile shapes. As discussed by D22 (in particular their section 4.2 and fig. 6), our 1D dense-shell models exhibit a dip as well as a blue-red asymmetry in essentially all strong lines (i.e. He I lines but also those of Mg II). This arises from a moderate continuum optical-depth effect (the blue-red asymmetry) as well as a line optical depth effect quenching the emission from the regions in the dense shell located in the mid-plane (at line-of-sight velocities near zero). This feature occurs in many similar dense-shell models and affects H_I lines in H-rich models. However, this feature is not observed at similar epochs, even in observations of SNe Ibn at high resolution and high S/N (e.g. SN 2006jc; Foley et al. 2007). One way of reducing such optical-depth effects in the model is to break up the dense shell into radially- and laterally-confined clumps. The 2D broken-shell models of clumped WR winds carried out by

Flores, Hillier & Dessart (2023) indicate that clumping can resolve this feature. Conversely, the lack of blue-red asymmetry and central dip in He I line profiles of observed SNe Ibn suggests that the dense shell that forms in those interactions is significantly clumped.

3.3 Composition and unique spectral line diagnostics

In numerous SNe IIn, the thermalized shock radiation within the dense shell at the interface between ejecta and CSM escapes predominantly in the UV, where a multitude of resonance lines of ions with different ionization potentials provide constraints on the abundances of both iron-group and intermediate-mass elements (e.g. Fransson et al. 2005; Groh 2014). Furthermore, the composition alters the colour through the changes in metal line blanketing and plasma cooling processes. The line-profile morphology also constrains the dynamics and geometry (e.g. Dessart & Hillier 2011). In the context of SN 2020nxt, the NUV range does not reveal such a variety of lines because of the much cooler gas and its low ionization at the epochs observed. Despite its low abundance, Fe (essentially at solar metallicity) represents the strongest coolant for the gas. This is in stark contrast from standard SN ejecta at nebular times where the low gas density favours the formation of strong forbidden lines that dominate the cooling. Here, because of the material compression associated with the interaction, such lines do not form. At earlier times, when a fraction of the CSM has not been shocked and compressed but is instead lower density slow gas influenced by the radiation injected at the shock, the SN may emit a much bluer spectrum with lines from ions with a high ionization potential.

The flux of a few dominant emission lines has been measured (after subtracting the continuum) for line diagnostics. For the Mg II doublet around 7891 Å and the Ca II triplet around 8542 Å that largely overlap, the flux in the whole line region is taken into account. We integrate flux in the range 4000–5500 Å to approximate the total flux of Fe II emission lines. Owing to its complicated and extended profile, the Fe II emission continuum is indistinguishable from the underlying blackbody continuum, so the result is unavoidably an overestimation of the real flux of Fe II emission. However, beyond \sim 15 d after peak, the emission lines gradually dominate the spectra as the continuum fades, so the total optical flux below 5500 Å can serve as a good approximation of the Fe line emission at later phases. A few relatively weak lines, such as He I 4471, may also contribute to the systematic bias in measuring Fe II emission. The left panel of Fig. 15 shows the ratios between the flux intensity of the continuum dominated by Fe II emission lines below 5500 Å and He I 5876, 7065 Å at different epochs, and the right panel shows the evolution of the flux ratio between He I 5876 Å and the Mg II doublet or the Ca II triplet. We also include the ratio measured from the simulation as discussed in Section 3 following the same line-measurement scheme.

The [Fe/He I] ratio decreases with time as the underlying continuum weakens and He I features become stronger, gradually levelling off after $\sim\!\!20\,d$ with ratios still $\gtrsim 20$. This feature shows the dominance of Fe II emission as the major coolant throughout all phases. Other trends include the fading of the Mg II doublets and the increase in the Ca II flux. After $\sim\!\!30\,d$, there is no obvious evolution in any of these line ratios.

In general, the model predictions agree with observations quantitatively except for a few systematic biases. At $\sim 10\,\mathrm{d}$ after peak brightness, all of the line ratios in Fig. 15 are underestimated, likely caused by the fact that He I is largely overestimated at early phases. As discussed in Section 3, such a systematic bias is likely caused by our oversimplified assumption of a narrow dense shell in the modelling. Another issue is that the model fails to reproduce the

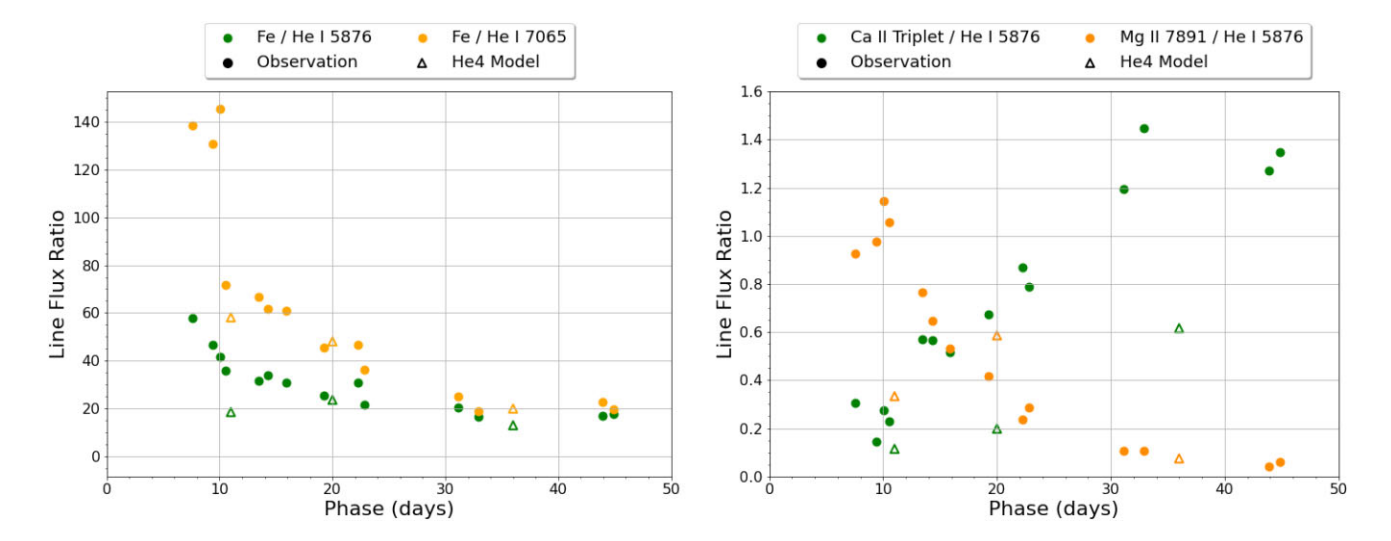


Figure 15. Left: The evolution of the line flux ratio between Fe II continuum below 5500 Å and the prominent He I 5876 Å. Right: The evolution of the line flux ratio between Mg II 7891 Å, the Ca II triplet around 8542 Å, and the prominent He I 5876 Å. The phases are relative to the o-band peak.

Ca II triplet, as can be seen from the first panel of Fig. 10. Such an effect can now be explained by an ionization effect, as discussed in Section 3. Overall, the model predictions show an excellent match with the observations, given the oversimplified assumptions used.

3.4 Model implications and discussion

The best-fitting model for SN 2020nxt is a moderate-mass He star powered by interaction. We show some good matches for a He-star model of 4 M_☉ initially on the He ZAMS, which corresponds to a pre-SN star mass of 3.16 M_{\odot} and a mass of 18.11 M_{\odot} on the H ZAMS. We have not covered the full parameter space of composition, powers, and locations for the shell, but tests have shown that the persistence of He I lines at all epochs requires a large He mass fraction relative to the total mass. Given the modest mass of the He-rich shell (i.e, the He/C and the He/N shells) of $\sim 1 M_{\odot}$ in massive stars at the time of core collapse (D22, Fig. 1), this constraint suggests that the total pre-SN mass cannot be much greater than $3-4 \,\mathrm{M}_{\odot}$. This effectively excludes massive stars with $M > 18 \,\mathrm{M}_\odot$ on the H ZAMS such as WR stars and points instead to lower mass massive stars that, in addition, have evolved in an interacting binary and lost their H-rich envelope through mass transfer from even lower mass stars. This type of binary interaction is required, since red supergiant winds are too weak to remove the H envelope in this initial mass range (Beasor et al. 2020; Beasor, Davies & Smith 2021). It also opens the possibility that some SNe Ibn arise instead from low-mass stars such as He white dwarfs.

The models presented in this work constrain the physical conditions necessary to generate the spectra, namely the presence of a high-mass helium envelope and a relatively helium-rich star (i.e. >80 per cent). These models do not directly constrain the nature of the envelope ejection in SN 2020nxt or any SN Ibn, although such a helium-rich system is exceptionally rare and limits the possible mechanisms, which include unstable mass transfer and nuclear flashes.

Extending the CMFGEN models to other fast transients, such as SNe Icn and FBOTs, is enticing because a small CSM shell around such SNe can naturally produce other fast luminous transients. For H-free ejecta, the mass of CSM that one expects from a massive star tends to be smaller than typically encountered in H-rich mass stars. Furthermore, metal-rich (or H-free) ejecta are poor donors of

free electrons and thus have a lower electron-scattering opacity (the associated mass-absorption coefficient is reduced by a factor of a few to a few tens). Consequently, the CSM has a lower optical depth and traps radiation for a shorter period, naturally leading to shorter rise times. If one assumes a similar energy injection from kinetic energy of the inner ejecta in the interaction scenario, this implies a greater peak luminosity. For example, radiating at $10^{43} \, \mathrm{erg \, s^{-1}}$ for $100 \, \mathrm{days}$ is energetically identical to radiating $10^{44} \, \mathrm{erg \, s^{-1}}$ for $10 \, \mathrm{dor} \, 10^{45} \, \mathrm{erg \, s^{-1}}$ for $1 \, \mathrm{d}$. The critical energy constraint is not the peak luminosity but the time integral of the bolometric luminosity. One may thus expect a natural trend for greater luminosity for shorter lived transients (see section 3 and fig. 3 of D22).

But such assumptions may be oversimplifying the situation. The composition and geometry of these other systems likely changes substantially. Furthermore, the presence of hydrogen in FBOTs points towards the likely explosion of a more massive star or a non-supernova event (e.g. tidal disruption event), while the lack of both hydrogen and helium in a Type Icn SN makes it difficult for CMFGEN models to constrain any progenitor mass. A physical relationship may indeed exist between the different classes of fast transients, but they may also simply be related by the fact that brief circumstellar interaction drives the shape and speed of the light curve around peak brightness. Additional multiwavelength observations may still be a useful tool, especially in the UV, where resonance lines with very high optical depths allow us to probe a larger range in radii.

4 CONCLUSIONS

We present multiwavelength observations of the Type Ibn SN 2020nxt. In addition, a comparison is provided of its spectroscopic evolution to the state-of-the-art radiative-transfer simulations based on D22, supporting a He-star progenitor of $4\,\mathrm{M}_\odot$ initially on the He ZAMS that lost its $\sim 1\,\mathrm{M}_\odot$ He-rich envelope in the years prior to explosion. There are discrepancies in reproducing the UV flux, some line ratios, and the line profiles, but there is hope in solving these issues with a more realistic, 3D interaction model of a clumpy dense shell. From the analysis of the pre-SN light curve in the ATLAS o band within 3 yr of the SN discovery, no signature of a pre-SN eruption has been found with a limiting magnitude of $M_{threshold} = -15$

mag for short pre-explosion eruption with 5 d duration or $M_{\rm threshold} = -13.5$ mag for long pre-explosion eruption with 100 d duration. The relatively low mass of the progenitor star disfavours the single massive star scenario, indicating that the progenitor system is likely to be an interacting binary system in which CSM may arise from the mass-transfer process. This result is consistent with low-mass progenitor star models for three other SNe Ibn fit by D22: SNe 2006jc, 2011hw, and 2018bcc.

UV spectra were important in this work. In addition to the spectroscopic evolution, we show that a fundamental quantity of interest is the fraction of the total kinetic energy that has been extracted from the impacting shell. This fractional kinetic energy is radiated, typically on a diffusion timescale, and produces the bolometric light curve of the SN. Because the emitting interaction region is often hot and ionized, a significant fraction of that radiation falls in the UV range and can be critical for differentiating between progenitor models (i.e. Fig. 11). The UV spectra were also key to securing the identification of Fe II line forest as the main contributor to the emission below 5500 Å, emphasizing that this Fe II emission actually extends down to 1000 Å where it vanishes. SNe Ibn are known for this strong emission in the blue part of the optical, and it is clearly not related to continuum emission; if that had been the case, the flux would have been much stronger in the UV.

Although very challenging, earlier UV will better help constrain the progenitors of SNe Ibn and FBOTs. At earlier phases (i.e. around or before bolometric maximum), the underlying continuum would have been stronger in the UV and the ionization likely would have been higher, at a time when the optical spectrum tends to be blue and featureless (e.g. like in FBOTs). It is at such times that lines for He II, C III, C IV, or NV could be seen in the UV, at a time when the optical spectrum tends to be blue and featureless (e.g. like in FBOTs).

In summary, these results provide an important perspective on the broader conversation about the evolutionary pathways of strippedenvelope SNe. Like non-interacting SNe Ib/c, the progenitor star likely went through multiple eruptions or interaction process to lose its H envelope and form massive He rich CSM around it (though such activities were not detected in the pre-SN ATLAS light curve). At the same time, the H-free CSM around such SNe can naturally produce other fast luminous transients like SNe Icn or FBOTs that are featureless in optical but full of high ionization features in UV at early time. Thus, the early UV spectra will be a key to understand the physical nature of SNe Ibn, fast transients, and all stripped-envelope SNe in the future.

ACKNOWLEDGEMENTS

Funding for this programme was provided by NASA/HST grant AR-14295 from the Space Telescope Science Institute (STScI), which is operated by the Association of Universities for Research in Astronomy (AURA), Inc., under National Aeronautics and Space Administration (NASA) contract NAS5-26555.

The data presented here were obtained in part with ALFOSC, which is provided by the Instituto de Astrofisica de Andalucia (IAA) under a joint agreement with the University of Copenhagen and NOT. This work makes use of data taken with the Las Cumbres Observatory global telescope network. The LCO group is funded by National Science Foundation (NSF) grants AST-1911151 and AST-1911225.

TS has been supported by the János Bolyai Research Scholarship of the Hungarian Academy of Sciences, as well as by the FK134432 grant of the National Research, Development and Innovation Office of Hungary and the ÚNKP 22–5 New National Excellence Programs

of the Ministry for Culture and Innovation from the source of the National Research, Development and Innovation Fund. AVF's supernova group at UC Berkeley has been supported by the Christopher R. Redlich Fund, Gary and Cynthia Bengier, William Draper, Timothy and Melissa Draper, Alan Eustace, Sanford Robertson, Clark and Sharon Winslow, Briggs and Kathleen Wood, and numerous other donors. P.K. is supported by NSF grant AST-1908823. CG and DF are supported by a VILLUM FONDEN Young Investigator Grant (project number 25501). This research was supported by the Munich Institute for Astro-, Particle and BioPhysics (MIAPbP) which is funded by the Deutsche Forschungsgemeinschaft (DFG, German Research Foundation) under Germany's Excellence Strategy – EXC-2094 - 390783311.

YSE-PZ was developed by the UC Santa Cruz Transients Team. The UCSC team is supported in part by NASA grants NNG17PX03C, 80NSSC19K1386, and 80NSSC20K0953; NSF grants AST-1518052, AST-1815935, and AST-1911206; the Gordon & Betty Moore Foundation; the Heising–Simons Foundation; a fellowship from the David and Lucile Packard Foundation to R.J. Foley; Gordon and Betty Moore Foundation postdoctoral fellowships and a NASA Einstein Fellowship, as administered through the NASA Hubble Fellowship programme and grant *HST*-HF2-51462.001, to D.O. Jones; and an NSF Graduate Research Fellowship, administered through grant DGE-1339067, to D.A. Coulter.

KAIT and its ongoing operation at Lick Observatory were made possible by donations from Sun Microsystems, Inc., the Hewlett-Packard Company, AutoScope Corporation, Lick Observatory, the NSF, the University of California, the Sylvia & Jim Katzman Foundation, and the TABASGO Foundation. A major upgrade of the Kast spectrograph on the Shane 3 m telescope at Lick Observatory was made possible through generous gifts from William and Marina Kast as well as the Heising-Simons Foundation. The authors acknowledge the help of James Sunseri, Matt Chu, Michael May, Nachiket Girish, Raphael Baer-Way, Teagan Chapman, Andrew Hoffman, and Asia deGraw in obtaining Lick Nickel 1 m data. Research at Lick Observatory is partially supported by a generous gift from Google.

The Young Supernova Experiment (YSE) and its research infrastructure is supported by the European Research Council under the European Union's Horizon 2020 research and innovation programme (ERC Grant Agreement 101002652, PI K. Mandel), the Heising-Simons Foundation (2018-0913, PI R. Foley; 2018-0911, PI R. Margutti), NASA (NNG17PX03C, PI R. Foley), NSF (AST-1720756, AST-1815935, PI R. Foley; AST-1909796, AST-1944985, PI R. Margutti), the David & Lucille Packard Foundation (PI R. Foley), VILLUM FONDEN (project 16599, PI J. Hjorth), and the Center for AstroPhysical Surveys (CAPS) at the National Center for Supercomputing Applications (NCSA) and the University of Illinois Urbana-Champaign.

A subset of the data presented herein were obtained at the W. M. Keck Observatory. NASA Keck time is administered by the NASA Exoplanet Science Institute. Keck data presented herein were from telescope time allocated to NASA through the agency's scientific partnership with the California Institute of Technology and the University of California. The Observatory was made possible by the generous financial support of the W. M. Keck Foundation. The authors wish to recognize and acknowledge the very significant cultural role and reverence that the summit of Maunakea has always had within the indigenous Hawaiian community. We are most fortunate to have the opportunity to conduct observations from this mountain.

Pan-STARRS is a project of the Institute for Astronomy of the University of Hawaii, and is supported by the NASA SSO Near Earth Observation Program under grants 80NSSC18K0971, NNX14AM74G, NNX12AR65G, NNX13AQ47G, NNX08AR22G, 80NSSC21K1572, and by the State of Hawaii. The Pan-STARRS1 Surveys (PS1) and the PS1 public science archive have been made possible through contributions by the Institute for Astronomy, the University of Hawaii, the Pan-STARRS Project Office, the Max-Planck Society and its participating institutes, the Max Planck Institute for Astronomy, Heidelberg and the Max Planck Institute for Extraterrestrial Physics, Garching, The Johns Hopkins University, Durham University, the University of Edinburgh, the Queen's University Belfast, the Harvard-Smithsonian Center for Astrophysics, the Las Cumbres Observatory Global Telescope Network Incorporated, the National Central University of Taiwan, STScI, NASA under grant NNX08AR22G issued through the Planetary Science Division of the NASA Science Mission Directorate, NSF grant AST-1238877, the University of Maryland, Eotvos Lorand University (ELTE), the Los Alamos National Laboratory, and the Gordon and Betty Moore Foundation.

We appreciate the excellent assistance of the staffs at the various observatories where data were obtained.

DATA AVAILABILITY

The data underlying this article will be shared on reasonable request to the corresponding author.

REFERENCES

```
P.D., Aleo, et al., 2023, The Astrophysical Journal Supplement Series, 266, 9
Beasor E. R., Davies B., Smith N., van Loon J. T., Gehrz R. D., Figer D. F., 2020, MNRAS, 492, 5994
```

Beasor E. R., Davies B., Smith N., 2021, ApJ, 922, 55

Brown P. J. et al., 2009, AJ, 137, 4517

Brown T. M. et al., 2013, PASP, 125, 1031

Brown P. J., Breeveld A. A., Holland S., Kuin P., Pritchard T., 2014, Ap&SS, 354, 89

Chambers K. C. et al., 2016, preprint (arXiv:1612.05560)

Chen Y. et al., 2023, ApJ, 955, 42

Coulter D. A. et al., 2022, YSE-PZ: An Open-source Target and Observation Management System. Zenodo.

Coulter D. A. et al., 2023, PASP, 135, 064501

Cushing M. C., Vacca W. D., Rayner J. T., 2004, PASP, 116, 362

Davis K. W. et al., 2022, MNRAS, 523, 2530

Dessart L., Hillier D. J., 2011, MNRAS, 415, 3497

Dessart L., Audit E., Hillier D. J., 2015, MNRAS, 449, 4304

Dessart L., Hillier D. J., Audit E., Livne E., Waldman R., 2016, MNRAS, 458, 2094

Dessart L., John Hillier D., Kuncarayakti H., 2022, A&A, 658, A130

Dewi J. D. M., Pols O. R., 2003, MNRAS, 344, 629

Djupvik A. A., Andersen J., 2010, Astrophys. Space Sci. Proc., 14, 211

Drout M. R. et al., 2014, ApJ, 794, 23

Filippenko A. V., 1982, PASP, 94, 715

Filippenko A. V., 1997, ARA&A, 35, 309

Filippenko A. V., Li W. D., Treffers R. R., Modjaz M., 2001, in Paczynski B., Chen W.-P., Lemme C., eds, ASP Conf. Ser. Vol. 246, IAU Colloq. 183: Small Telescope Astronomy on Global Scales. Astron. Soc. Pac., San Francisco, p. 121

Flewelling H. A. et al., 2020, ApJS, 251, 7

Flores B. L., Hillier D. J., Dessart L., 2023, MNRAS, 518, 5001

Foley R. J. et al., 2003, PASP, 115, 1220

Foley R. J., Smith N., Ganeshalingam M., Li W., Chornock R., Filippenko A. V., 2007, ApJ, 657, L105

Fox O. D., Smith N., 2019, MNRAS, 488, 3772

Fransson C. et al., 2005, ApJ, 622, 991

Gal-Yam A. et al., 2022, Nature, 601, 201

```
Galbany L. et al., 2018, ApJ, 855, 107
```

Gaskell C. M., Cappellaro E., Dinerstein H. L., Garnett D. R., Harkness R. P., Wheeler J. C., 1986, ApJ, 306, L77

Gehrels N. et al., 2004, ApJ, 611, 1005

Groh J. H., 2014, A&A, 572, L11

Guevel D., Hosseinzadeh G., 2017, Dguevel/Pyzogy: Initial Release, Zenodo.

Ho A. Y. Q. et al., 2023, ApJ, 949, 120

Ho A. Y. Q. et al., 2023, Nature, 623, 927

Horne K., 1986, PASP, 98, 609

Hosseinzadeh G. et al., 2017, ApJ, 836, 158

Hosseinzadeh G., McCully C., Zabludoff A. I., Arcavi I., French K. D., Howell D. A., Berger E., Hiramatsu D., 2019, ApJ, 871, L9

Jacobson-Galán W. V. et al., 2022, ApJ, 924, 15

Jones D. O. et al., 2021a, ApJ, 908, 143

Jones D. O. et al., 2021b, ApJ, 908, 143

Karamehmetoglu E. et al., 2021, A&A, 649, A163

Kennicutt R. C., Jr, 1998, ARA&A, 36, 189

Landolt A. U., 1983, AJ, 88, 439

Landolt A. U., 1992, AJ, 104, 340

Langer N., 2012, ARA&A, 50, 107

Li W., Filippenko A. V., Chornock R., Jha S., 2003, PASP, 115, 844

Lyutikov M., Toonen S., 2019, MNRAS, 487, 5618

Magnier E. A. et al., 2020a, ApJS, 251, 3

Magnier E. A. et al., 2020b, ApJS, 251, 5

Magnier E. A. et al., 2020c, ApJS, 251, 6

Margutti R. et al., 2019, ApJ, 872, 18

McCully C., Volgenau N. H., Harbeck D.-R., Lister T. A., Saunders E. S., Turner M. L., Siiverd R. J., Bowman M., 2018, in Guzman J. C., Ibsen J., eds, Proc. SPIE Conf. Ser. Vol. 10707, Software and Cyber Infrastructure for Astronomy V. SPIE, Bellingham, p. 107070K

Metzger B. D., 2022, ApJ, 932, 84

Metzger B. D., Giannios D., Thompson T. A., Bucciantini N., Quataert E., 2011, MNRAS, 413, 2031

Miller J., Stone R., 1993, Lick Observatory Technical Report 66, Univ. California.

Nicholl M., 2018, Res. Notes Am. Astron. Soc., 2, 230

Ofek E. O. et al., 2014, ApJ, 789, 104

Oke J. B., Gunn J. E., 1983, ApJ, 266, 713

Oke J. B. et al., 1995, PASP, 107, 375

Paschalidis V., Etienne Z., Liu Y. T., Shapiro S. L., 2011, Phys. Rev. D, 83, 064002

Pastorello A. et al., 2007, Nature, 447, 829

Pastorello A. et al., 2008a, MNRAS, 389, 113

Pastorello A. et al., 2008b, MNRAS, 389, 131

Pastorello A. et al., 2015a, MNRAS, 449, 1921 Pastorello A. et al., 2015b, MNRAS, 449, 1954

Pastorello A. et al., 2015c, MNRAS, 454, 4293

Pastorello A. et al., 2015c, MNRAS, 454, 4293

Pellegrino C. et al., 2022, ApJ, 938, 73

Perley D. A. et al., 2022, ApJ, 927, 180

Podsiadlowski P., Joss P. C., Hsu J. J. L., 1992, ApJ, 391, 246

Pols O. R., 1994, A&A, 290, 119

Prochaska J. X. et al., 2020a, pypeit/PypeIt: Release 1.0.0., Zenodo.

Prochaska J. et al., 2020b, J. Open Source Softw., 5, 2308

Rest S. et al., 2021, in American Astronomical Society Meeting Abstracts. p. 551.16

Rest S. et al., 2023, ATClean: High-Fidelity, Statistically Clean AT-LAS Light Curves and Feature Detection, Zenodo.

Riess A. G. et al., 2022, ApJ, 934, L7

Roming P. W. A. et al., 2005, Space Sci. Rev., 120, 95

SDSS Collaboration et al., 2017, ApJS, 233, 25

Schlafly E. F., Finkbeiner D. P., 2011, ApJ, 737, 103

Schlegel E. M., 1990, MNRAS, 244, 269

Shivvers I. et al., 2017, MNRAS, 471, 4381

Siebert M. R., Dimitriadis G., Polin A., Foley R. J., 2020, ApJ, 900, L27

Silverman J. M. et al., 2012, MNRAS, 425, 1789

Smith N., 2014, ARA&A, 52, 487

Smith N., 2017, in Alsabti A. W., Murdin P., eds, Handbook of Supernovae, Springer, Cham, Switzerland. p. 403

- Smith N., Arnett W. D., 2014, ApJ, 785, 82
- Smith N., Foley R. J., Filippenko A. V., 2008, ApJ, 680, 568
- Smith N., Li W., Silverman J. M., Ganeshalingam M., Filippenko A. V., 2011, MNRAS, 415, 773
- Smith K. W. et al., 2020, PASP, 132, 085002
- Srivastav S., Smartt S. J., McBrien O., Smith K. W., Young D. R., Gillanders J., 2020, Transient Name Server Classification Report, 2020-2148, 1
- Stahl B. E. et al., 2019, MNRAS, 490, 3882
- Stetson P. B., 1987, Astron. Soc. Pac., 99, 191
- Strotjohann N. L. et al., 2021, ApJ, 907, 99
- Sun N.-C., Maund J. R., Hirai R., Crowther P. A., Podsiadlowski P., 2020, MNRAS, 491, 6000
- Sun N.-C., Maund J. R., Crowther P. A., 2023, MNRAS, 521, 2860
- Tauris T. M., Langer N., Moriya T. J., Podsiadlowski P., Yoon S. C., Blinnikov S. I., 2013, ApJ, 778, L23
- Tonry J. L. et al., 2012, ApJ, 750, 99
- Tonry J. et al., 2018a, PASP, 130, 064505
- Tonry J. L. et al., 2018b, ApJ, 867, 105
- Tonry J. et al., 2020, Transient Name Server Discovery Report, 2020-2022, 1
- Valenti S. et al., 2014, MNRAS, 438, L101
- Valenti S. et al., 2016, MNRAS, 459, 3939
- Waters C. Z. et al., 2020, ApJS, 251, 4
- Wilson J. C. et al., 2004, in Moorwood A. F. M., Iye M., eds, SPIE Conf. Ser. Vol. 5492, Ground-based Instrumentation for Astronomy. SPIE, Bellingham, p. 1295
- Woosley S. E., 2019, ApJ, 878, 49
- Woosley S. E., Heger A., 2015, ApJ, 810, 34
- Yao Y. et al., 2022, ApJ, 934, 104
- Yaron O., Gal-Yam A., 2012, PASP, 124, 668

SUPPORTING INFORMATION

Supplementary data are available at MNRAS online.

Please note: Oxford University Press is not responsible for the content or functionality of any supporting materials supplied by the authors. Any queries (other than missing material) should be directed to the corresponding author for the article.

- ¹Physics and Astronomy Department, Johns Hopkins University, Baltimore, MD 21218, USA
- ²Space Telescope Science Institute, 3700 San Martin Drive, Baltimore, MD 21218, USA
- ³Department of Physics and Astronomy, University of Kansas, Lawrence, KS 66045, USA
- ⁴Institut d'Astrophysique de Paris, CNRS-Sorbonne Université, 98 bis boulevard Arago, F-75014 Paris, France
- ⁵Department of Computer Science, Johns Hopkins University, Baltimore, MD 21218, USA
- ⁶School of Physics, Trinity College Dublin, The University of Dublin, Dublin 2. Ireland
- ⁷Department of Astronomy, Oskar Klein Centre, Stockholm University, AlbaNova, SE-106 91 Stockholm, Sweden

- ⁸Steward Observatory, University of Arizona, 933 N. Cherry Ave., Tucson, AZ 85721, USA
- ⁹Department of Astronomy, University of California, Berkeley, CA 94720, USA
- ¹⁰Gemini Observatory, 670 North A'ohoku Place, Hilo, HI 96720, USA
- ¹¹ Department of Physics and Astronomy, Texas A&M University, 4242 TAMU, College Station, TX 77843, USA
- ¹²George P. and Cynthia Woods Mitchell Institute for Fundamental Physics & Astronomy, College Station, TX 77843, USA
- ¹³Las Cumbres Observatory, 6740 Cortona Drive, Suite 102, Goleta, CA 93117, USA
- ¹⁴Department of Physics, University of California, Santa Barbara, CA 93106, USA
- ¹⁵Department of Astronomy, University of Virginia, PO Box 400325, Charlottesville, VA 22904, USA
- ¹⁶Department of Physics & Astronomy, Louisiana State University, Baton Rouge, LA 70803, USA
- ¹⁷Department of Astronomy and Astrophysics, University of California, Santa Cruz, CA 95064, USA
- ¹⁸Department of Physics and Astronomy, Michigan State University, East Lansing, MI 48824, USA
- ¹⁹Center for Astrophysics | Harvard & Smithsonian, 60 Garden Street, Cambridge, MA 02138, USA
- ²⁰The NSF AI Institute for Artificial Intelligence and Fundamental Interactions, Massachusetts Institute of Technology, 77 Massachusetts Ave, Cambridge MA 02139, USA
- ²¹Department of Physics and Astronomy, Rutgers the State University of New Jersey, 136 Frelinghuysen Road, Piscataway, NJ 08854, USA
- ²²Division of Physics, Mathematics, and Astronomy, California Institute of Technology, Pasadena, CA 91125, USA
- ²³Minnesota Institute for Astrophysics, University of Minnesota, 115 Union St. SE, Minneapolis, MN 55455, USA
- ²⁴Department of Physics and Astronomy, Northwestern University, 2145 Sheridan Rd, Evanston, IL 60208, USA
- ²⁵Center for Interdisciplinary Exploration and Research in Astrophysics (CIERA), Northwestern University, 1800 Sherman Ave, Evanston, IL 60201, USA
- ²⁶Department of Experimental Physics, University of Szeged, H-6720 Szeged, Dóm tér 9., Hungary
- ²⁷ELKH-SZTE Stellar Astrophysics Research Group, H-6500 Baja, Szegedi út, Kt. 766, Hungary
- ²⁸National Astronomical Research Institute of Thailand, 260 Moo 4, Donkaew, Maerim, Chiang Mai 50180, Thailand
- ²⁹Caltech/IPAC, Mailcode 100-22, Pasadena, CA 91125, USA
- ³⁰Institute for Astronomy, University of Hawaii, 2680 Woodlawn Drive, Honolulu, HI 96822, USA
- ³¹Department of Astronomy, University of Illinois at Urbana-Champaign, 1002 W. Green Str. IL 61801, USA
- ³²DARK, Niels Bohr Institute, University of Copenhagen, Jagtvej 128, 2200 Copenhagen, Denmark
- ³³Department of Astronomy & Astrophysics, The Pennsylvania State University, University Park, PA 16802, USA

This paper has been typeset from a TEX/LATEX file prepared by the author.